International Journal of Biological Macromolecules 263 (2024) 130154

Contents lists available at ScienceDirect

International Journal of Biological Macromolecules

journal homepage: www.elsevier.com/locate/ijbiomac

# Nanofibers of *N*,*N*,*N*-trimethyl chitosan capped bimetallic nanoparticles: Preparation, characterization, wound dressing and in vivo treatment of MDR microbial infection and tracking by optical and photoacoustic imaging

Ankit Kumar Malik [a], Chandrashekhar Singh [a], Punit Tiwari [b], Dipti Verma [c], Abhishesh Kumar Mehata [a], Vikas [a], Aseem Setia [a], Ashim Mukherjee [c], Madaswamy S. Muthu [a,*]

[a] Department of Pharmaceutical Engineering and Technology, Indian Institute of Technology (BHU), Varanasi 221005, UP, India
[b] Department of Microbiology, Institute of Medical Sciences, BHU, Varanasi 221005, UP, India
[c] Department of Molecular and Human Genetics, Institute of Science, Banaras Hindu University, Varanasi 221005, UP, India

ARTICLE INFO

*Keywords:*
Antimicrobial resistance
Bimetallic nanoparticles-nanofibers
*Pseudomonas aeruginosa*
Photoacoustic imaging
Trimethyl chitosan
Wound dressing

ABSTRACT

Recent advancements in wound care have led to the development of interactive wound dressings utilizing nanotechnology, aimed at enhancing healing and combating bacterial infections while adhering to established protocols. Our novel wound dressings consist of *N*,*N*,*N*-trimethyl chitosan capped gold-silver nanoparticles (Au-Ag-TMC-NPs), with a mean size of 108.3 ± 8.4 nm and a zeta potential of +54.4 ± 1.8 mV. These optimized nanoparticles exhibit potent antibacterial and antifungal properties, with minimum inhibitory concentrations ranging from 0.390 μg $ml^{-1}$ to 3.125 μg $ml^{-1}$ and also exhibited promising zones of inhibition against multi-drug resistant strains of *S. aureus*, *E. coli*, *P. aeruginosa*, and *C. albicans*. Microbial transmission electron microscopy reveals substantial damage to cell walls and DNA condensation post-treatment. Furthermore, the nanoparticles demonstrate remarkable inhibition of microbial efflux pumps and are non-hemolytic in human blood. Incorporated into polyvinyl alcohol/chitosan nanofibers, they form Au-Ag-TMC-NPs-NFs with diameters of 100–350 nm, facilitating efficient antimicrobial wound dressing. In vivo studies on MDR microbial-infected wounds in mice showed 99.34 % wound healing rate within 12 days, corroborated by analyses of wound marker protein expression levels and advanced imaging techniques such as ultrasound/photoacoustic imaging, providing real-time visualization and blood flow assessment for a comprehensive understanding of the dynamic wound healing processes.

## 1. Introduction

*N*,*N*,*N*-Trimethyl chitosan (TMC) $(C_9H_{18}ClNO_4)_n$ (low molecular weight, degree of quaternization >50 %) is a hydrophilic quaternized form of chitosan, drawing considerable attention for its solubility and exceptional antibacterial activity across a wide range of pH levels, owing to the presence of positively charged N-atoms [1–3]. The antimicrobial activity of chitosan and its derivatives stems from their ability to form complexes with the cell envelope [4–6] or disrupt gene expressions [7]. A higher abundance of positive charges renders TMC more potent in terms of antibacterial activity. Consequently, the emergence of versatile wound dressings with TMC properties and antibacterial activity has gained significant popularity in recent times [5].

There is currently a pervasive concern over the proliferation of contagious pathogenic germs. The existing antibiotics possess several limitations, underscoring the necessity of developing superior and more adaptable substances to combat bacterial illnesses [8]. Antimicrobial resistance (AMR) has become a serious public health concern in the 21st century, characterized by the emergence of bacterial strains that have evolved to withstand the therapeutic effects of drugs often employed for disease treatment. Based on the findings of the review on AMR, a study commissioned by the UK Government, it is projected that by the year 2050, there would be a substantial increase in the number of deaths caused by AMR, reaching an estimated yearly total of 10 million

* Corresponding author.
*E-mail address:* msmuthu.phe@itbhu.ac.in (M.S. Muthu).

https://doi.org/10.1016/j.ijbiomac.2024.130154
Received 25 November 2023; Received in revised form 26 January 2024; Accepted 11 February 2024
Available online 13 February 2024

fatalities [9,10].

Specifically, the prevalence of multidrug resistance (MDR) is now widespread among well-known pathogens. MDR in bacteria refers to their ability to withstand the effects of multiple antimicrobial drugs, compromising the efficacy of standard treatments. In the year 2019, around 929,000 deaths worldwide were attributed to six prominent infections, namely *Escherichia coli*, *Klebsiella pneumonia, Pseudomonas aeruginosa, Acinetobacter baumannii, Staphylococcus aureus* and *Streptococcus pneumoniae* [11]. Nevertheless, current research has revealed an escalation in the prevalence MDR strains of bacteria (*Escherichia coli, Pseudomonas aeruginosa and Staphylococcus aureus)* and fungal (*Candida albicans)* species, exhibiting resistance to most prescribed drugs [12,13].

Nanofibers possess a structure that closely resembles the natural extracellular matrix (ECM), characterized by a significant surface area and high porosity. This structure enables the efficient transport of vital nutrients and metabolites required for cellular development. Nanofibers has the ability to provide a favourable setting for cellular adhesion, proliferation, and growth [14,15]. In certain biomedical applications, such as tissue regeneration, a significant challenge and critical concern is achieving a continuous and controlled release of active compounds or growth factors. Nanoparticles loaded nanofibers composites have received much attention as a potential solution to this problem. Thus, nanofibers are considered a promising material for wound dressing, with potential applications in the treatment of diverse injuries and infections. Recently, nanofiber dressings consisting of nanoparticles have gained popularity due to their ability to fulfill the complicated needs of the biological environment at the site of bacterial infection, which standard nanofiber dressings are unable to fulfill [16].

Among metallic nanoparticles those consisting of gold and silver exhibit exceptional stability [17,18]. In addition to its antibacterial capabilities, gold nanoparticles have been the focus of extensive study. In contrast, silver nanoparticles have received great interest in academic study owing to their tremendous potential in antibacterial applications [19–21]. One notable benefit of using this particular technique is its ability to use a minimal dose of therapeutic agent in combination of the other therapeutic agent for potentiating the treatment outcomes against MDR microbes. It has already been showed that the nanoformulation containing Ag-NPs is crucial for their bactericidal efficacy [22]. The antimicrobial activity is mainly attributed to the release mechanism of $Ag^{+}$ ion. To enhance the antimicrobial sustainability of nanoparticles preferred to be embedded in porous matrices nanofibers, which allows the controlled release and prolonged acting therapeutic agent from the extracellular matrix to the MDR bacterial infected wound site [23]. This include the re-organization of the cytoskeleton, the decrease in the expression of components of epithelial junctional, and increase in the gene expressions responsible for facilitating cytoskeletal modifications and adhesion to mesenchymal cells. These unique approaches give the ability to boost wound healing outcomes and reduce impediments.

This research specifically addresses the issue of antimicrobial resistance, which is one of the top 10 global public health threats. More specifically, it focuses on the problem of MDR microbial infected wound. The synthetic antimicrobial agents currently available in the market no longer have a significant effect on these MDR microbes. Additionally, prolonged use of antimicrobial agents leads to the development of resistance in the microbes [11]. Given the insufficiency of efficient antibiotics, metallic nanoparticles have been used as an alternative.

In this study, primarily TMC capped gold-silver nanoparticles (Au-Ag-TMC-NPs) were reported first time for antimicrobial wound dressing and in vivo wound healing activity. Secondly, Au-Ag-TMC-NPs were encapsulated for the first time within a polyvinyl alcohol and chitosan-based nanofiber matrix (Au-Ag-TMC-NPs-NFs) for potential in vivo wound healing applications. Treating microbial resistant wounds with low or no adverse effects has proven to be a challenging task. In an effort to address this issue, we have developed Au-Ag-TMC-NPs-NFs for in vivo wound healing applications. Initially, developed Au-Ag-TMC-NPs were characterized for particle size, zeta potential, poly dispersity index, surface morphology, and elemental analysis. Notably, Au-Ag-TMC-NPs antimicrobial activity against MDR strains of *E. coli, P. aeruginosa, S. aureus* and *C. albicans* were evaluated through in vitro experiments in comparison to the marketed broad spectrum antibiotic. Additionally, the antimicrobial mode of action of Au-Ag-TMC-NPs was examined for anti-efflux pump activity by employing gene expression profiling. Moreover, the molecular mechanism of accelerated wound healing was explained by signaling pathway protein expression levels. The Au-Ag-TMC-NPs were evenly dispersed into Au-Ag-TMC-NPs-NFs matrix by using the process of electrospinning. The nanofibers were then applied on MDR microbes-infected mice wound sites. The wound healing potency of nanofibers was assessed by the wound closures, re-epithelization, wound marker protein expression levels and ultrasound/photoacoustic imaging. Likewise, the real time wound visualization, angiogenesis, vascularity, and wound oxygen saturation were also evaluated.

## 2. Materials and methods

### 2.1. Materials

Gold (III) chloride trihydrate ($HAuCl_4 \cdot 3H_2O$) and silver nitrate ($AgNO_3$), *N*,*N*,*N*-trimethyl chitosan $(C_9H_{18}ClNO_4)n$ (low molecular weight, degree of quaternization >50 %), polyvinyl alcohol $(C_2H_4O)n$, and tween 80. Chitosan (MW ~ 30 kDa, degree of deacetylation ≥90 %) was procured from Sisco Research Laboratory Pvt. Ltd. Microbiological media (Muller Hinton broth (MHB) and Muller Hinton agar (MHA) medium) was bought from HiMedia Laboratories, Pvt. Ltd. India. LIVE/DEAD BacLight Bacterial Viability Kit (L7012) was purchased from Molecular Probes, Invitrogen (Grand Island, NY, USA). DiD'dye (DiIC18 (5) oil (1,1'-Dioctadecyl-3,3,3′,3'-Tetramethylindodicarbocyanine Perchlorate)) was purchased from Thermo Fisher Scientific, Mumbai, India. β-Actin (13E5) Rabbit mAb (45 kDa), Vimentin (D21H3) XP® Rabbit mAb (57 kDa), Phospho-p44/42-MAPK-(Erk1/2)-(Thr202/Tyr204) (D13.14.4E) XP® Rabbit mAb (44, 42 kDa) were bought from Cell Signaling Technology (Beverly, MA). TGF-β1 polyclonal antibody (44 kDa) (Cat. No.:*E*-AB-33090) was purchased from Elabscience Biotechnology (USA). All the chemicals used in the present research were of analytical grade.

### 2.2. Synthesis and characterization of Au-Ag-TMC-NPs

The synthesis of gold-silver core-shell nanoparticles will be carried out using a seeded growth synthesis approach, where Au nanoparticles will be utilized as the seed material [24]. Concisely, pre-synthesized 1 ml gold nanoparticles subjected into 9 ml of distilled water at 80 °C. Varying molar ratios of $HAuCl_4 \cdot 3H_2O$ and $AgNO_3$ (1:0.5, 1:1, 1:2 and 1:3) and concurrently 0.1 % 10 ml of TMC solution (as reducing and capping agent) were placed and maintained on a magnetic stirrer at 80 °C. The solution colour changes from pink to dark brown within 20–25 min supporting the formation of Au—Ag nanoparticles. An additional hour was allocated for the completion of the reaction. Followed by the conjugation with TMC in the presence of resuspending agent (Tween80) to avoid particle clustering during purifying process. In brief, 5 ml (2 mg/ml) TMC aqueous solution of 1 % (*w/v*) Tween-80 was formulated in distilled water. Following that, 1.8 ml (1 mg/ml) of Sodium tri-poly-phosphate (TPP) solution (pH 8) was gently subjected drop wise to the solution of TMC (pH 6) while stirring at 37 °C, resulting in a final pH of roughly 7. To accomplish a comparative analysis of the antibacterial properties shown by Au-Ag-TMC-NPs, an additional five formulations were prepared as gold nanoparticles (Au-NPs), TMC based gold nanoparticles (Au-TMC-NPs), silver nanoparticles (Ag-NPs), TMC based silver nanoparticles (Ag-TMC-NPs), and gold-silver nanoparticles (Au-Ag-NPs). Nano formulation of various batches are presented in Table S1.

#### 2.2.1. Particle size, poly-dispersity index, and surface charge

The hydrodynamic particle size (PS), poly dispersity index (PDI) of the optimized nanoparticles by using the principle of dynamic light scattering was assessed using the Malvern Zetasizer (Nanoseries). Whereas surface charge was measured by electrophoretic light scattering principle.

#### 2.2.2. UV-spectroscopy

The UV–visible spectra of all batches of optimized nanoparticles were obtained using a spectrophotometer (Shimadzu-1800). The UV–Visible absorbance spectra was measured by scanning the nanoparticles in the wavelength range of 300–700 nm [24]. The instrument's spectral bandwidth was adjusted to 1/10 of the scanning rate, was of 1200 nm/min.

#### 2.2.3. Transmission electron microscopy (TEM) analysis

The investigation of the shape, size and morphology of the optimized nanoparticles at nanoscale was conducted by TEM analysis (Tecnai G2 20 TWIN). The specimens were made using the drop-casting technique, without the utilisation of staining agents. The nanoparticles that had been optimized were subjected to sonication for a duration of 5 min. Subsequent to their dilution in distilled water. A liquid droplet was deposited onto a TEM grid made of carbon-coated copper with a mesh size of 400. The droplet was allowed to dry for an extended period of time before being subjected to examination [25].

#### 2.2.4. Atomic force microscopy (AFM) analysis

The investigation of the optimized nanoparticles form and morphology was conducted using AFM (NT-MDT Service & Logistics Ltd). The specimens were prepared following dilution with ultrapure water. Following a sonication period of 5 min., a small amount of prepared samples was placed onto a microscope slide measuring 1 × 1 cm and subsequently allowed to dry for a duration of 24 h. The NOVA programme, developed by NT-MDT, was utilized for image processing in order to acquire 2D and 3D AFM pictures of the optimized nanoparticles.

#### 2.2.5. STEM-EDX analysis

The Au-Ag-TMC-NPs were subjected to investigation using Energy Dispersive X-ray investigation (EDX) to identify the constituent components.

### 2.3. Antimicrobial activity

#### 2.3.1. Isolation of multidrug-resistant microorganism

Strain of multidrug-resistant gram-negative bacteria *E. coli* and *P. aeruginosa*, gram-positive bacteria *S. aureus* and gram-positive fungus *C. albicans* were isolated from environmental samples and waste of Sir Sunderlal Hospital, BHU, Varanasi, Uttar Pradesh, India and other local hospitals. The selected strains were then subjected to an overnight incubation in Luria–Bertani (LB) medium at 37 °C to facilitate their complete growth and confirmed by measuring the absorbance at $\lambda_{max}$ of 550 nm after centrifuging the samples at 5000 rpm for 12 min. In each experiment, a single colony of multidrug resistant bacteria was picked from the agar plate and cultured at 37 °C, 200 rpm for 12 h in LB-medium [26,27].

#### 2.3.2. Estimation of MIC, MBC and MFC

Minimum inhibitory concentration (MIC) is the lowest concentration of an antimicrobial agent that prohibits observable growth of bacteria, confirming the drug's capacity to suppress microbial proliferation. Meanwhile, minimum bactericidal concentration (MBC) and minimum fungicidal concentration (MFC) is the lowest concentration of an antibiotic and antifungal that causes in the death of a specific percentage of bacterial and fungal cells, demonstrating the agent's potential to kill the bacteria and fungus rather than only prevent their development. All the optimized nanoparticles were subjected for the determination of MIC, MBC, and MFC against the strains of gram-positive and gram-negative microbial strains (each containing $10^7$–$10^8$ CFU/ml microbe) in a 96-well culture plates. Microbial strains introduced into a liquid broth medium of different concentrations of all the optimized nanoparticles (200 μg $ml^{-1}$-0.097 μg $ml^{-1}$) by using 2-fold serial dilution method. The values of MIC were determined by assessing the minimal concentration of the optimized nanoparticles which effectively inhibits bacterial cell proliferation. The use of the MBC and MFC serves as a valuable adjunct to the MIC assay. The objective of this research was to evaluate the minimum concentration of the formulations required to decrease the viability of the original bacterial and fungal inoculum to 100 %.

#### 2.3.3. Disc diffusion assay

The experiment of disc diffusion assay was used to evaluate the antimicrobial susceptibility of the optimized nanoparticles against both grams' microbial strains. Mueller Hinton agar plates have been made by spreading the Mueller Hinton Broth cultured microbial media [28]. The sterile Whatman paper (grade-1) of 5 mm discs' diameter were saturated with optimized nanoparticles and a standard antibiotic (Ciprofloxacin). These discs were then carefully placed onto the surface of separate MHA plates containing strains of both grams' microbial strains using sterilized forceps. The plates were subsequently incubated at a temperature of 37 °C for an overnight period. The ZOI was measured in diameter (mm) by using conventional measuring scale. This was done to evaluate the resistance and compare the effectiveness of all optimized nanoparticles with the standard medication.

#### 2.3.4. Anti-biofilm activity

To evaluate the anti-biofilm efficacy of the optimized nanoparticles against the microbial strains, glass slides measuring 1.3 $cm^2$ were utilized as a substrate for the drop-casting biofilm deposition (200 μg $ml^{-1}$–0.097 μg $ml^{-1}$). The dispersion undergoing dripping was subjected to a drying process for a duration of 24 h at a temperature of 37 °C, which was then followed by an additional hour of drying at a temperature of 70 °C. The biofilm of the bacterial strain that was not subjected to any treatment was used as the control in the experiment. The shape of bacterial biofilm treated with optimized nanoparticles was investigated using SEM using the MA15/18 model from Carl Zeiss Microscopy Ltd [29,30]. In each well of a 12 well culture microplate with a round coverslip, 500 μl of a bacterial cell culture in log phase and 500 μl of different amounts of test chemicals (specifically optimized nanoparticles) were introduced. The round coverslips underwent a washing process using phosphate buffer saline (PBS) and were then fixed with a glutaraldehyde solution of 2.5 % for a duration of 3 h at a temperature of 4 °C. Prior to this fixation step, the coverslips were incubated at a temperature of 37 °C for a period of 24 h. The biofilm adhered to the round coverslip was then introduced to dehydration at a 4 °C for 10 min., using an ethyl alcohol gradient with progressively rising concentrations (25 %, 50 %, 70 %, 90 %, and 100 %, respectively). Prior to conducting SEM analysis, the round coverslips underwent a drying process and were afterwards protected with a layer of carbon by utilizing sputter coating technique.

#### 2.3.5. Live-dead cell viability assay

The confocal laser scanning microscopy (CLSM) technique was used to investigate the microbial viability test. The objective is to ascertain the proportion of viable and non-viable cells by utilizing the LIVE-DEAD Bac-Light microbial viability gear [31]. As per the guidelines outlined in the Bac-Light™ microbial viability gear user manual, the mixture of stain was administered in one of three ways: (1) directly applied to surfaces covered with biofilm, where the stain mix was diluted with PBS and pipetted onto the surfaces, subsequently shielded with a coverslip; (2) applied to microbial cells taken off from the surfaces utilizing ultrasonography; or (3) applied to microbes collected from the upper layer of the microbial biofilms. The stained samples underwent incubation for a duration of 15 min. at ambient temperature under conditions of

darkness.

### 2.3.6. TEM microscopy of microbes

TEM is a potent technique used to examine the structural properties, internal organization, and interactions of microbes with their surrounding environment. The microbial cells in the control group (untreated) and the group treated with Au-Ag-TMC-NPs (optimized concentration for the respective microbe) were subjected to two washes with PBS (pH 7.4). Afterward, they were fixed with 2.5 % (*v*/v) glutaraldehyde, subsequent to post-fixation using 1 % osmium tetraoxide. Finally, the cells were then washed again with PBS (pH 7.4) [32]. Moreover, the specimens underwent a slow dehydration process with the progressive augmentation of ethanol concentration. The thin slices were prepared with an ultra-microtome instrument (Leica; model- UC7) equipped with a diamond knife, followed by subsequently affixed onto copper grids [33]. The sections above were promptly analyzed following their preparation utilizing TEM with cryogenic capabilities (CRYO-TEM (TALOS S), Thermo Scientific) operating at an accelerating voltage of 80 Kilovolts.

### 2.3.7. Atomic force microscopy of microbes

The acquisition of AFM pictures was performed on cells that were placed onto glass slides (NTEGRA Prima-NT-MDT Service & Logistics Ltd). When it comes to analysing the biochemical and material aspects of filamentous structures formed by live bacterial cells in aqueous environments, AFM is an effective tool [34]. A micro cantilever with a sharp probing tip at its end is used to do horizontal line scans across a surface. When the cantilever's tip makes contact with a surface, it causes the device to bend, producing a topographic map. Sub-molecular resolution nano-scale topographical pictures of surface features under physiological circumstances and with little sample preparation are achieved. The microbial cells used for AFM imaging were cultivated on surfaces that had been pre-treated with Au-Ag-TMC-NPs (optimized concentration for the respective microbe) at time interval of 0 h, 06 h and 12 h, followed by washing with PBS for 24 h at 37 °C, before AFM imaging, Microorganisms that exhibited poor adhesion to the glass surface were subjected to thorough rinsing using a generous amount of milli-Q water. Subsequently, they were air-dried in a controlled atmosphere with a relative humidity of 30 %. The experiment used silicon nitride cantilevers (Olympus AC240TS) with specific parameters. The cantilevers were operated at a scan speed of 1 Hz, with a frequency of resonance ranging from 80 to 100 kHz. Additionally, the cantilevers had a curvature radius of 30 nm and a stiffness value of 5 N/m [35].

## 2.4. Efflux pump gene expression profiling by semi-quantitative analysis (RT-PCR)

Semi-quantitative RT-PCR was performed using extracted RNA from microbial isolates were cultured in the presence of a sub-inhibitory optimized concentration of nanoparticles for respective microbe as well as an untreated negative control. RNA was extracted using the QIAamp RNeasy mini gear (Qiagen GmbH, Germany) manuals provided by the manufacturer. RNA isolation was assessed for integrity via agarose gel electrophoresis. The cDNA product obtained from reverse transcription of the RNA was subjected to semi-quantitative PCR analysis and which was initiated with a denaturation step of 100 °C for 2 min, followed by 20 cycles of 60 s each for denaturation at 94 °C, annealing at 56 °C for 20 s, and extension at 72 °C for 1 min, with the last extension at 80 °C for 10 min. Primer sequences were specific to the genes coding for the main efflux pump of the microbes shown in Table 1 and were designed using Primer3 software and the PCR products were visualized under UV light on a 1.2 % (*w*/*v*) agarose gel. All gene expressions were compared and *ampC* gene was used as a housekeeping gene for internal control for Semi q-RT PCR [36,37]. The genBank accession numbers for the used primers are as follow *acrA*: HQ833334 [38]; *acrB*: MT956578 [39]; *MexA*: ON920994 [40]; *MexB*: NC002516 [41]; *norA*: CP011526 [42]; *norB*: MN013174 [43]; *ERG11*: XM711729 [44]; *TAC1*: OQ383350 [45]; ampC: ON920993 [46]. Quantification of the PCR products was done densitometrically using Image J software.

**Table 1**
Primers used in semi-quantitative RT-PCR.

| Microbes | Genes | Primer sequence | nMoles |
|---|---|---|---|
| MDR *E. coli.* | *acrA*-F | 5′- CTCTCAGGCAGCTTAGCCCTAA −3’ | 39.4 |
| | *acrA*-R | 5′- TGCAGAGGTTCAGTTTTGACTTT −3’ | 35.0 |
| | *acrB*-F | 5′- AAGAAGCTACCCGTAAGTCG −3’ | 25.9 |
| | *acrB*-R | 5′- AGTAGAACCGCCAAAGAAGG −3’ | 30.3 |
| MDR *P. aeruginosa* | *MexA*-F | 5′- ACCTACGAGGCCGACTACCAGA −3’ | 33.7 |
| | *MexA*-R | 5′- GTTGGTCACCAGGGCGCCTTC -3’ | 31.5 |
| | *MexB*-F | 5′- GTGTTCGGCTCGCAGTACTC -3’ | 35.6 |
| | *MexB*-R | 5′- AACCGTCGGGATTGACCTTG −3’ | 41.3 |
| MDR *S. aureus* | *norA*-F | 5′- TGTTAAGTCTTGGTCATCTGCA −3’ | 31.3 |
| | *norA*-R | 5′- CCATAAATCCACCAATCCC -3’ | 25.4 |
| | *norB*-F | 5′- ATGGAAAAGCCGTCAAGAGA −3’ | 26.2 |
| | *norB*-R | 5′- AACCAATGATTGTGCAAATAGC -3’ | 33.6 |
| MDR *Candida albicans* | *ERG11*-F | 5′- ACCCTGAAGATTTTGATCCAACTAGATG-3’ | 24.3 |
| | *ERG11*-R | 5′- CCCAAACCCATAATCAACTTCATCAGA −3’ | 23.0 |
| | *TAC1*-F | 5′ - TGGCAATGTATTTAGCAGATGAGG −3’ | 16.5 |
| | *TAC1*-R | 5′ - TGCTTGAACTGAGGTGAATTTTG −3’ | 19.9 |
| Housekeeping gene | *ampC-F* | 5′- GGTGCAGAAGGACCAGGCACAGAT-3’ | 31.2 |
| | *ampC-R* | 5′- CGATGCTCGGGTTGGAATAGAGGC-3’ | 35.6 |

## 2.5. Hemolysis test

The assessment of the hemolytic capacity is crucial in order to guarantee the safety of nanoparticles when applied to wounds, distilled water, saline, Au-NPs, Au-TMC-NPs, Ag-NPs, Ag-TMC-NPs and Au-Ag-TMC-NPs were used for the comparison. Human blood was drawn from healthy volunteers, and plasma was separated by centrifugation, followed by three PBS washes. Concisely 200 μL of washed blood was added along with 800 μL of each nanoparticle sample [47]. Follwed by incubation of all tubes for 2 h at 37 °C then centrifuged at 3000 rpm for 8 min was done, and 100 μL of the supernatant was then subjected to 96-well plates and the absorbance was recorded at 540 nm. The percentages of hemolysis were computed using the eq. 1:

$$\%\text{Hemolysis} = \frac{\text{Optical density of test} - \text{Optical density of PBS}}{\text{Optical density of distilled water} - \text{Optical density of PBS}} \times 100 \quad (1)$$

## 2.6. Preparation and characterization of Au-Ag-TMC-NPs-NFs nanofibers

A 4 % solution (*w*/*v*) of Chitosan (CS) was prepared by dissolving it in a binary solvent system consisting of acetic acid and distilled water (80/20 ratio) at a temperature of 80 °C, using magnetic stirring. Polyvinyl alcohol (PVA) solutions with a weight concentration of 5 % were generated by disintegrating PVA powder in distilled water in controlled conditions, ensuring a constant temperature of 70 °C. The chitosan 4 wt %-PVA 5 wt% solution was prepared by combining CS and PVA solutions in a 1:1 volume ratio [48]. Further, Au-Ag-TMC-NPs solution (1 mL) was introduced to CS-PVA solution (2.5 mL). The CS-PVA-Au-Ag-TMC-NPs mixture was subjected to intense stirring for 2 h. The uniform gel obtained was used for the processes of drop-casting or electrospinning.

### 2.6.1. Electrospinning process

During a conventional electrospinning procedure, a mixture containing CS-PVA-Au-Ag-TMC-NPs was introduced into a syringe pump

and subjected to electrospinning under a positive voltage of 15 kV. The distance between the target and the tip of the needle used for collection was 12 cm. The collection plate used in the experiment was a grounded aluminium foil. The flow rate was consistently maintained at 0.4 mL/h, the rotating drum speed was set at 5000 rpm, and the electrospinning process was conducted for a duration of 3 h [49].

#### 2.6.2. Contact angle measurement

The water contact angle analyzed by using an instrument First-Ten-Angstroms, Portsmouth, VA, USA was used. Electrospun nanofibers membrane samples (1 cm × 1 cm) were removed and introduced on a testing plate, and then distilled water was poured onto the surfaces of the membranes [50]. Camera measurements were used to compare the contact angles of blank nanofibers with those of Au-Ag-TMC-NPs-NFs.

#### 2.6.3. FT-IR analysis

The FT-IR technology was used to investigate the various functional moieties present in the electrospun nanofibers by using Nicolet iS5 of THERMO Electron Scientific Instruments LLC within the range of 4000–500 $cm^{-1}$ wavenumber.

#### 2.6.4. XRD analysis

The XRD examination of electrospun nanofibers were conducted utilizing a Bench Top X-Ray Diffraction instrument (BT-XRD: RIGAKU Corporation).

#### 2.6.5. TEM analysis

Nanofibers spun in a coaxial direction were spread out on a copper TEM grid for a field emission TEM analysis (Tecnai G2 20 TWIN).

#### 2.6.6. SEM analysis

The examination of the morphology of nanofibers was conducted using a field emission SEM subsequent to the application of carbon sputtering (model EVO-Scanning Electron Microscope MA15/18, Carl Zeiss Microscopy Ltd.)

#### 2.6.7. AFM analysis

Topography and morphology of electrospun nanofibers were analyzed using NTEGRA Prima of NT-MDT Service & Logistics Ltd. (SNL/10, silicon tip with nitride lever). Droplets of the aqueous nanofiber solution were vacuum dried on mica for 8 h before being scanned in Scan-Asyst-peak force tapping style in an ambient air environment. AFM utilizes a scanning mechanism equipped with a Silicon (Si) cantilever that is positioned vertically adjacent to the sample. The resonant frequency of the cantilever, which represents its natural oscillation frequency when not influenced by external forces, is employed as the driving frequency for the scanning process.

#### 2.6.8. Water retention capacity

By immersing the nanofibers in a PBS solution (pH 7.4) for 48 h at 37 °C, we determined the nanofibers ability to hold water. The samples were taken out of the solution at predetermined intervals, blotted dry using tissue paper, and then weighed on the precision electronic weighing scale [51,52]. Triplicates of each samples were tested. The percentage of water retention was calculated using Eq. (2):

$$\text{Water retention } (\%) = \left(\frac{\text{Wwet} - \text{Wdry}}{\text{Wdry}}\right) \times 100 \quad (2)$$

where, $W_{dry}$ and $W_{wet}$ are the dry and wet sample weights, respectively, before and after being submerged in the PBS solution.

#### 2.6.9. Nanofiber stability and degradation

The investigation focused on the stability and deterioration of the nanofibers via the process of immersing the samples in the PBS (pH 7.4) and lysozyme solution (105 U/mL in water) at 37 °C. Degradation of lysozyme was monitored for up to 20 days, during which time the lysozyme solution was replaced every 3 days. At the 10th and 20th day, Subsequently, specimens were extracted from the solution and subjected to two rounds of rinsing with distilled water [51]. The Eq. (3) used to determine the percentage of deterioration is as follows:

$$\text{Degradation } (\%) = \left(\frac{\text{Wi} - \text{Wf}}{\text{Wi}}\right) \times 100 \quad (3)$$

where, the $W_i$ and $W_f$ were pre-degradation and post-degradation sample weights, respectively.

#### 2.6.10. Thermal stability

Thermogravimetric analysis was performed on electrospun nanofibers via TGA-50 model of M/s Shimadzu (Asia-Pacific) Pte Ltd. The experiments were conducted at heating rates of 10 °C/min, ranging from an initial temperature of 30 °C to a final temperature of 700 °C.

#### 2.6.11. In-vitro release study

The dialysis bag diffusion technique was used to assess the release profile of $Ag^+$ and Au from the produced Au-Ag-TMC-NPs and Au-Ag-TMC-NPs-NFs. In a concise manner, a volume of 1 ml of Au-Ag-TMC-NPs was placed into a dialysis bag with a molecular weight cutoff of 1 kD and thereafter sealed in an airtight manner. On the other hand, Au-Ag-TMC-NPs-NFs was cut into smaller pieces (1 cm × 1 cm), approximately 10 mg of the sample were submerged in 1 ml of PBS (pH 7.4) at a temperature of 37 °C. The sample was then placed into a dialysis bag with a molecular weight cutoff of 1 kD and securely sealed. The dialysis bag was submerged in a glass flask containing 100 mL of PBS medium (pH 7.4). The whole experimental apparatus was positioned inside a water-bath shaker (Remi CM-12 Plus, Vasai) set at a temperature of 37 ± 0.5 °C, while maintaining a constant shaking motion [53]. According to the pre-established time-intervals of 1 h, 2 h, 3 h, 6 h, 8 h, 12 h, 24 h, and 48 h, 1 mL samples were collected and an equivalent amount of fresh medium was added. Subsequently, the samples underwent analysis by UV–visible spectroscopy at a 517 nm wavelength. The concentration of the unknown material was determined by employing a pre-established standard calibration curve ($R^2$ = 0.9902) specific to the Au—Ag bimetallic complex.

#### 2.6.12. Hemolysis study of nanofibers

Nanofibers were put through a hemolysis test to see if they were safe for human use. The ability of red blood cells (erythrocytes) to break down and release haemoglobin into plasma was measured in this assay. Dressings are divided into three categories based on their index of hemolysis, as defined by ASTM F 756-00 (2000) [54]: (1) The use of a hemolytic dressing, resulting in a hemolysis rate above 5 %, (2) The dressing has a modest hemolytic effect, characterized by a hemolysis rate ranging from 2 % to 5 %; and (3) The dressing under consideration is non-hemolytic, as shown by its hemolytic index of 2 % [55]. The hemolysis produced by Au-Ag-TMC-NPs-NFs was compared with distilled water, saline and Au-Ag-TMC-NPs on healthy erythrocytes.

#### 2.6.13. Whole blood clotting ability

In order to assess the hemostatic properties of the nanofibers, the nanofiber film was placed separately in glass petri dishes and preheated to a temperature of 37 °C [56]. Subsequently, 200 μL of fresh human blood was applied onto the surface of each film, and an additional 30 μL of 0.2 M $CaCl_2$ solution was introduced to commence the process of coagulation. The petri-plates holding the nanofibers were then incubated at 37 °C for 10 min. Followed by 10 min incubation period, 30 mL of distilled water was carefully introduced drop by drop to all petri-plates avoiding disrupting the clot. This procedure was conducted in order to facilitate the hemolysis of red blood cells that were not entrapped inside the clot, using a volume of 25 mL of water. Following this, the measurement of absorbance was conducted on the resultant

solution of haemoglobin at a specific wavelength of 540 nm.

#### 2.6.14. Thrombus development analysis

Gravimetric analysis was utilized to investigate thrombus development on nanofibers [57]. In the usual procedure, the nanofiber film (1 × 1 cm), was immersed in a solution of saline for a duration of 24 h at a temperature of 37 °C. Followed by the extraction of nanofiber from solution of saline and then exposed to 1.5 mL of acid citrate dextrose blood, which was carefully applied onto the surface of the nanofibers. Followed by the introduction of 20 μL of a 0.2 M calcium chloride solution to induce the development of a thrombus within a time frame of around 3–4 min. The process of thrombus development was halted by the introduction of 8 ml distilled water at the mark of 20 min. Clot was then immersed in a 40 % solution of formalin (10 ml) for a duration of 10 min. Ultimately, the immobilized clot was rinsed with water, gently dried with soaking paper, and afterwards weight was measured.

### 2.7. In-vivo study of Au-Ag-TMC-NPs-NFs distribution on wound site

In-vivo fluorescence optical imaging of blank nanofiber with free-DiD (control), Au-Ag-TMC-NPs-NFs-DiD was performed on uninfected and different microbial infected wounds in mice utilizing the Photon-Imager-Optima-System (Biospace Lab). The free-DiD and DiD tagged Au-Ag-TMC-NPs-NFs equivalent to 200 nM of DiD dye were applied to the wound, The fluorescence signals were recorded at excitation and emission wavelengths of 620 and 710 nm, respectively, after 10 min. At time intervals of 2, 4, 8, 24, and 48 h after the application. The analysis of radiant efficiency quantified as the ratio of fluorescence intensity to the product of area and time, was conducted using the imaging software provided by Biospace Lab. This analysis included using the region of interest (ROI) tool to surround the specific area of the wound.

### 2.8. Wound healing study

#### 2.8.1. In-vivo wound healing study

A wound healing potential study was performed in mice (Swiss albino, 18–22 g weight). The Institutional Animal Ethics Committee (IAEC) at the Indian Institute of Technology (Banaras Hindu University), Varanasi, UP, India, approved all in vivo animal experiments (IAEC Approval Number: IIT(BHU)/IAEC/2023/041) and the studies were carried out in compliance with the guidelines provided by the National Research Council's Guide for the Care and Use of Laboratory Animals. The animals were housed in controlled environments where temperature was regulated, humidity levels were maintained at a regular level, and a 12 h light/dark cycle was implemented. The mice ($n = 5$) were randomly assigned to seven different groups. The excision wound mice model was established by applying hair removal lotion to the dorsal region, followed by shaving. A circular region with an estimated size of about 314 $mm^2$ was generated subsequent to the administration of ketamine (50 mg/kg, body weight- i.p.) to anaesthetize the animals [24]. The wound of each of the seven mice groups was deliberately infected by introducing the corresponding MDR microorganisms onto the location of the lesion. In this study, a commercial formulation of ciprofloxacin ointment, which is a broad-spectrum antibiotic, was used as the positive-control. Conversely, the negative-control consisted of an untreated lesion. One cohort is maintained in a non-infected state and is undergoing treatment with the Au-Ag-TMC-NPs-NFs. Furthermore, several demographic cohorts are experiencing infections caused by distinct MDR microbial strains. The grouping of the experimental mice was as follows:

The experimental groups.

- Group I: The wounds of the mice were left untreated;
- Group II: The wounds of the mice were with marketed application of ciprofloxacin ointment USP of 0.3 % (*w*/w); a concentration;
- Group III: The wounds of the mice were keep uninfected and treated with the use of Au-Ag-TMC-NPs-NFs therapy (3.25 μg $ml^{-1}$);
- Group IV: The wounds of the mice were infected by the process of inoculation with the MDR *E. coli* bacteria on the wound sites followed by the treatment with Au-Ag-TMC-NPs-NFs (0.390 μg $ml^{-1}$);
- Group V: The wounds of the mice were infected by the process of inoculation with the MDR *Pseudomonas aeruginosa* bacteria on the wound sites followed by the treatment with Au-Ag-TMC-NPs-NFs (0.781 μg $ml^{-1}$);
- Group VI: The wounds of the mice were infected by the process of inoculation with the MDR *S. aureus* bacteria on the wound sites followed by the treatment with Au-Ag-TMC-NPs-NFs (0.195 μg $ml^{-1}$);
- Group VII: The wounds of the mice were infected by the process of inoculation with the MDR *Candida albicans* bacteria on the wound sites followed by the treatment with Au-Ag-TMC-NPs-NFs (3.125 μg $ml^{-1}$).

Treatment was delivered once a day from the beginning of the operation to the end of the recovery period. The software tool ImageJ was used to quantitatively assess the extent of wound healing over a period of time by the comparison of area of wound at a certain period with the initial area of wound. The relative percent area of the wound was plotted against time in order to get an understanding of the rate at which it was recovering.

#### 2.8.2. Histopathological studies

Following a period of 12 days, the mice in each respective groups sacrified by using $CO_2$ asphyxia. Subsequently, their layer of skin with wounds was carefully removed, and the resulting tissues were preserved in a solution of formalin with a concentration of 10 % *v*/v. Additionally, a rotary microtome was used to cut 10 μm thick slices of paraffin-embedded tissue. Staining with hematoxylin and eosin was employed to examine the tissue slices. A bright field microscope (Dewinter microscope) and Capture pro 4.1 software were used to observe the histological changes under the microscope [58].

### 2.9. In-vivo ultrasound/photoacoustic study

The wound model of mice was made after infection of the wound with MDR microbes was used for in vivo photoacoustic study. Then mice were divided into groups of seven, with each group consisting of three mice ($n = 3$). After that, all the animals were scanned under an ultrasound/photoacoustic imaging system (Vevo LAZR_X Vevo 3100, Toronto, Canada, 40 MHz ultrasound array transducer). The wound was scanned in B mode of ultrasound, for the vascularity study the power Doppler mode was on whereas for oxygenated/deoxygenated blood the photoacoustic mode was on. Photoacoustic/ultrasound imaging of the wound was visualized on $1^{st}$, $4^{th}$, $8^{th}$, and $12^{th}$ day post-treatment. The ultrasound/photoacoustic pictures were superimposed in order to ascertain the dimensions and oxygen saturation of the wound. Power Doppler image setting was done to analyzed wound vascularity. For the processing of images, the Vevo-LAB-software (FUZIFILM Visual Sonics, Toronto, Canada) was used [59].

### 2.10. Western blot study of wound marker protein

The western blot method was used to illustrate the manifestation of the wound healing marker proteins like the vimentin mesenchymal marker associated with epithelial-mesenchymal transition (EMT), SMAD2, and phospho MAPK (ERK 1/2) [58]. Wound skin tissues of untreated mice, and mice treated with marketed formulation, uninfected mice treated with Au-Ag-TMC-NPs-NFs, and microbial infected mice (MDR strains of *E. coli*, *P. aeruginosa*, *S. aureus*, and *C. albicans*) treated

with Au-Ag-TMC-NPs-NFs were dissected on ice. Approximately 5.0 mg of tissue was homogenized in 300 μl of ice-cold 1× RIPA lysis buffer (50 mM Tris–HCl pH 7.4, 1 % NP-40, 0.25 % sodium-deoxycholate, 150 mM NaCl, 1 mM EDTA) using electric homogenizer [60]. Protein concentration was measured by nanodrop (Thermo Scientific) and samples containing ~70 μg of protein were denatured and run at 12 % SDS-PAGE gel. Separation of the peptides on SDS-PAGE was followed by overnight transfer of proteins from the gel onto a PVDF membrane. Following the application of a 4 % skimmed milk solution in TBST, the blocking process was conducted, the membrane was incubated with primary antibody followed by AP-conjugated secondary antibody. Chromogenic detection of the signal was carried out using Sigma FAST NBT/BCIP. The primary antibodies used for western blotting were Rabbit anti-Vimentin (1:1000), Rabbit anti-Phospho SMAD2 (1:1000), Rabbit anti-Phospho MAPK (ERK 1/2) (1:2000), Rabbit anti-β Actin (1:1000). Expression of Vimentin was significantly increased in protein samples obtained from mice infected with MDR *P. aeruginosa* and treated with Au-Ag-TMC-NPs-NFs, in comparison to a control group of untreated animals. ImageJ was used for the analysis of the intensity of the protein bands.

### 2.11. Statistical analysis

All the in vivo and in vitro data were interpreted by using Graph Pad Prism 9.0 software. All the data was triplicated and presented as mean ± SD. Statistical significance among groups was calculated by One-Way ANOVA and *t*-test. The values ns ($p \geq 0.05$), * ($p < 0.05$), ** ($p < 0.01$), *** ($p < 0.001$), and **** ($p < 0.0001$) were considered for significance level determination.

## 3. Results and discussion

### 3.1. Characterization of nanoparticles

#### 3.1.1. Particle size, PDI and surface charge

The particle size, PDI and surface charge of synthesized nanoparticles were found to be in the range of 82.6 ± 4.8 nm to 133.7 ± 9.5 nm, 0.106 ± 0.082 to 0.239 ± 0.062 and 18.4 ± 2.5 mV to 54.4 ± 1.8 mV respectively (Table S2 and Fig. S1). Results revealed that uniformly dispersed Au-Ag-TMC-NPs possess a higher positive charge than their monometallic and bimetallic counterparts. Whereas all the TMC-based nanoparticle surfaces had charges between +45 and + 54 mV, demonstrating their high level of stability due to TMC [61].

#### 3.1.2. UV/Vis spectroscopy

The comparative UV–vis spectra of the synthesized nanoparticles are depicted in (Fig. S2). UV–vis spectra were observed in the range from 535 to 480 nm [62].

#### 3.1.3. Transmission electron microscopy (TEM) analysis

The TEM images of various synthesized nanoparticle formulations were observed at the resolution of 50 nm to 200 nm. The TEM images of Au-NPs, Ag-NPs and Au-Ag-NPs depict a clear and spherical geometry without any outer layer on the surface, whereas Au-Ag-NPs and Au-Ag-TMC-NPs reveal that deposition on the surface of the nanoparticles that could be interpreted as covering of TMC (Fig. 1A). The physical nature of all the nanoparticle formulations was examined by TEM-SAED (Selected Area Electron Diffraction) (Fig. 1B). The SAED image of Au-NPs, Ag-NPs depicts a regular pattern of bright spots, demonstrating its crystalline nature, whereas the SAED images of Ag-TMC-NPs, Au-Ag-NPs and Au-Ag-TMC-NPs formulation showed discrete rings and the spots with an irregular pattern which reveals their polycrystalline nature.

#### 3.1.4. Atomic force microscopy (AFM) analysis

The surface topography of the synthesized nanoparticle formulations was analyzed by the AFM, as demonstrated in (Fig. 1C, D) nanoparticles are round, smooth, and devoid of visible pinholes or fissures.

#### 3.1.5. STEM-EDX analysis

The Au-Ag-TMC-NPs were subjected to elemental analysis by STEM-EDX analysis, which conclusively verifies the existence of gold and silver metals. Fig. S3 illustrates a graphical depiction of the atomic proportion of Ag and Au is 85.59 % and 14.41 % respectively.

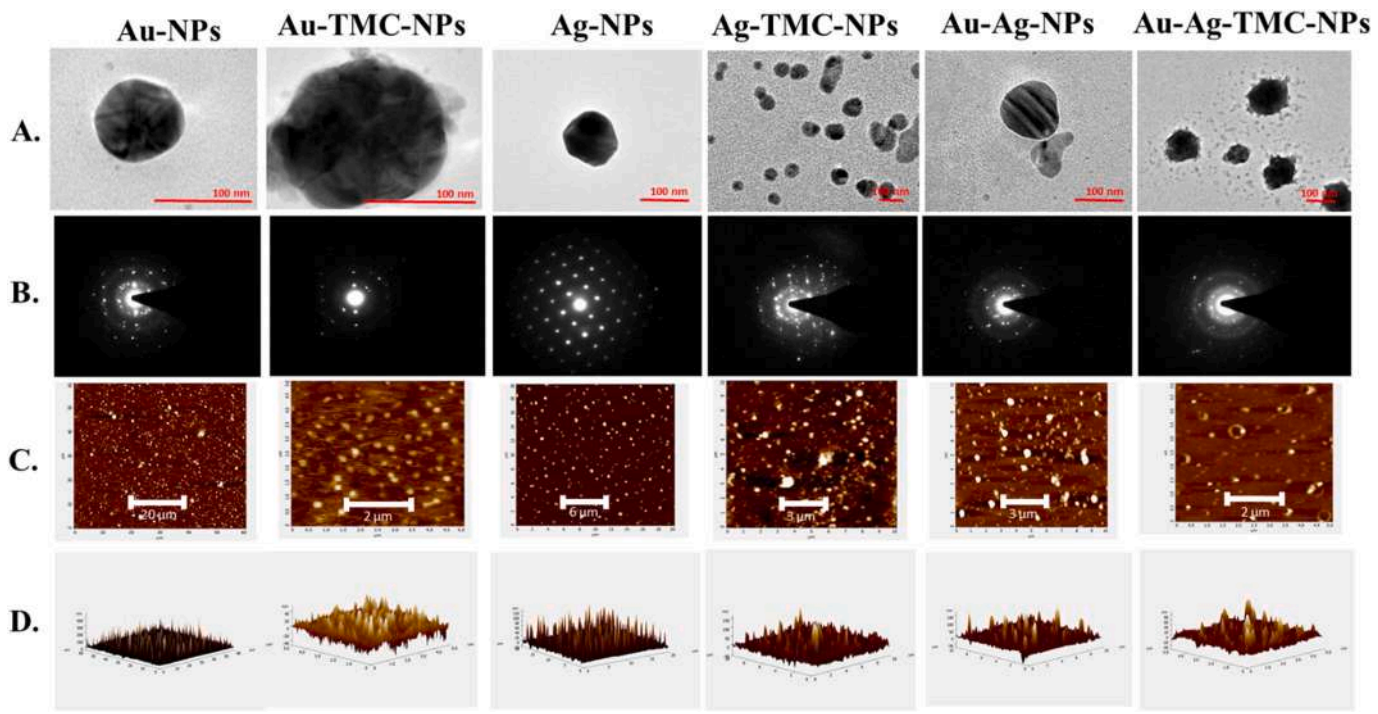


**Fig. 1.** (A) TEM, (B) SAED, (C) 2D AFM, (D) 3D AFM of synthesized nanoparticle formulations.

### 3.2. Antimicrobial activity of nanoparticles

#### 3.2.1. MIC, MBC and MFC

According to the MIC, MBC and MFC, the potential nanoformulation Au-Ag-TMC-NPs was found to be most effective among all the formulations, including marketed formulation for all the MDR microbial strains, by considering this, all the related studies will be carried out. For, Au-Ag-TMC-NPs, the ratio of MBC to MIC for MDR *E. coli* was found to 0.390 μg $ml^{-1}$/0.390 μg $ml^{-1}$ ⩽1, whereas for MDR *P. aeruginosa* it was 0.781 μg $ml^{-1}$ /0.781 μg $ml^{-1}$ ⩽1, whereas for MDR *S. aureus* it was 0.195 μg $ml^{-1}$ /0.390 μg $ml^{-1}$ ⩽2, and for MDR *C. albicans* it was 3.125 μg $ml^{-1}$ /3.125 μg $ml^{-1}$ ⩽1 (Table S3, Fig. S4). The MBC to MIC ratio is ⩽4 indicate more potent antibacterial agents [63]. This study demonstrates that the developed nanoformulation Au-Ag-TMC-NPs has superior antibacterial efficacy compared to other nanoformulations. Specifically, it shows significant promise in combating MDR of *S. aureus* and MDR *E. coli.* and MDR *P. aeruginosa* and MDR *C. albicans*.

#### 3.2.2. Bacterial susceptibility

The results obtained from the study demonstrated that Au-Ag-TMC-NPs showed maximum zone of inhibition among all other nanoformulations and antibiotic ciprofloxacin (Table 2). This experiment revealed that increasing the level of concentration (2-fold approx) of Au-Ag-TMC-NPs from 0.781 μg $ml^{-1}$ to 1.562 μg $ml^{-1}$ for MDR *P. aeruginosa*, 1.562 μg $ml^{-1}$ to 3.125 μg $ml^{-1}$ for MDR *E. coli*, 3.125 μg $ml^{-1}$ to 6.25 μg $ml^{-1}$ for MDR *S. aureus*, and 6.25 μg $ml^{-1}$ to 12.5 μg $ml^{-1}$ for MDR *Candida albicans*, the ZOI was slightly increased (Fig. S5). This study showed that the developed nanoformulation Au-Ag-TMC-NPs has great Bacterial susceptibility in comparison to other nanoformulations. Specifically, it shows significant promise in combating MDR of *S. aureus* and MDR *E. coli.* MDR *P. aeruginosa* and MDR *C. albicans*.

#### 3.2.3. Bacterial viability test

The assessment of bacterial viability was performed by live dead assay, after treatment with Au-Ag-TMC-NPs revealed that initially (0 h), the % of viable cells of MDR *E. coli* (Fig. 2A) was 52.14 ± 1.56 %. However, following a duration of 6 h, and 12 h of treatment, these % decreased significantly to 15.56 ± 0.10 % and 3.11 ± 0.11 %, respectively. Furthermore, for MDR *P. aeruginosa* (Fig. 2B) the viable cells were 88.03 ± 1.93 % in the beginning (0 h), but after 6 h, and 12 h treatment, they were found to be 24.13 ± 0.24 % and 0.76 ± 0.01 %, respectively. The visible cells for MDR *S. aureus* (Fig. 2C) were 75.54 ± 2.93 % in the beginning (0 h), but after 6 h, and 12 h treatment, they were found to be 30.13 ± 1.24 % and 5.76 ± 0.84 %, respectively. For MDR *C. albicans* (Fig. 2D) the viable cell count was 48.54 ± 2.64 % in the beginning (0 h), but after 6 h, and 12 h of treatment, they were found to be 31.13 ± 1.12 % and 8.76 ± 0.47 %, respectively. The quantification of living and dead cells in the individual CLSM pictures was performed using Image-J software, as seen in Fig. S6. Due to the increased surface free energy of the surface Ag atoms in the bimetallic NPs structure, Au—Ag core-shell NPs may have enhanced antibacterial characteristics [64]. The Au-Ag-TMC-NPs exhibited a substantial reduction in the count of live cells and concurrent rise in the count of dead cells when interacting with the MDR bacterial strains, demonstrating a strong antibacterial synergy.

#### 3.2.4. Antibiofilm activity

The electron micrograph of the test microorganism after treatment with Au-Ag-TMC-NPs treatment showed the damage of the biofilm over time. The findings of the SEM and AFM analysis provide confirmation that Au-Ag-TMC-NPs exhibit a significant antibiofilm action (Fig. 2A.1, B.1, C.1, D.1) (Fig. 3). The observed phenomenon might perhaps be attributed to the heightened infiltration of Au-Ag-TMC-NPs with positive charges, enhanced binding affinity to the biofilm. The results suggests upon exposure to NPs, a time-dependent decrease in biofilm development was seen in MDR strains. The Au-Ag-TMC-NPs are efficient against multidrug-resistant microbial cells in biofilms and effectively reduce the resistance of stationary bacterial and fungal cells to antimicrobial drugs [65,66].

#### 3.2.5. TEM microscopy study of test microbes

TEM microscopy investigation demonstrated that Au-Ag-TMC-NPs had time-dependent antibacterial activity against MDR microbial strains (Fig. 4). At 0 h, the MDR microbial strains cell walls were observed to be intact. After 12 h of treatment, the MDR *E. coli* and MDR *S. aureus* TEM visualization revealed that the cell walls became irregularly wavy, damaged, and the cell wall integrity was lost. Similar results were also observed in a recent study [24]. The TEM visualization of MDR *P. aeruginosa* surprisingly showed the absence of any disturbance in the external membrane but instead unveiled the condensation of DNA inside the bacterial cells [67]. The integrity of the MDR *C. albicans* cell wall was found to be intact, accompanied by alterations in the cellular composition [68]. The study's findings demonstrated that Au-Ag-TMC-NPs has the ability to effectively neutralise MDR microbial strains by damaging the cell wall integrity, by external membrane disturbance or by bacterial DNA condensation.

#### 3.2.6. Effect on the mRNA expression of biofilm-inducing efflux pump

The gene expression profiling of the efflux pump gene has been depicted in Fig. 5. The increased gene expression of the housekeeping gene *ampC* levels of the efflux pump in regards of all the targeted genes. The expression of *acrA* (67.01 ± 2.94 %) and *acrB* (82.94 ± 3.12 %) genes in MDR *E. coli* are downregulated. Likewise the downregulation of *MexA* (23.85 ± 1.47 %), *MexB* (28.13 ± 1.69 %), and *OprM* (31.84 ± 2.51 %) genes level of efflux pump in MDR *P. aeruginosa*. Also, the downregulation of *NorA* (42.75 ± 3.76 %) and *NorB* (57.78 ± 4.12 %) genes level of the efflux pump in MDR *S. aureus* were found. In MDR *Candida albicans,* the gene *ERG11* (93.73 ± 4.22 %), *TAC1* (84.54 ± 2.17 %) showed downregulation of genes expression level. All these efflux pump genes are essential for multidrug resistance in MDR *E. coli*, MDR *P. aeruginosa*, MDR *S. aureus* and MDR *Candida albicans* (Fig. 5A, B). The obtained results suggested that potential application of the developed Au-Ag-TMC-NPs formulation for inhibition of the MDR microbial efflux pumps activity. In the domain of MDR microbial strains, the downregulation of specific genes may have considerable repercussions for the organism's physiology and behavior. It may lead to

**Table 2**
Zone of inhibition of the optimized nanoparticles on various MDR microbes.

| Formulations | MDR *E. coli* | | MDR *P. aeruginosa* | | MDR *S. aureus* | | MDR *Candida albicans* | |
|---|---|---|---|---|---|---|---|---|
| | MIC (μg $ml^{-1}$) | ZOI (mm) | MIC (μg $ml^{-1}$) | ZOI (mm) | MIC (μg $ml^{-1}$) | ZOI (mm) | MIC (μg $ml^{-1}$) | ZOI (mm) |
| Au-NPs | 50 | 1.67 ± 0.21 | 100 | 0.70 ± 0.26 | 50 | 4.49 ± 0.12 | 200 | No zone |
| Au-TMC-NPs | 50 | 1.73 ± 0.14 | 100 | 1.03 ± 0.11 | 25 | 5.18 ± 0.10 | 200 | No zone |
| Ag-NPs | 12.5 | 12.02 ± 0.17 | 25 | 7.98 ± 0.07 | 12.5 | 10.66 ± 0.16 | 100 | 1.33 ± 0.15 |
| Ag-TMC-NPs | 12.5 | 13.96 ± 0.07 | 12.5 | 11.77 ± 0.17 | 6.25 | 12.6 ± 0.12 | 50 | 1.75 ± 0.08 |
| Au-Ag-NPs | 1.562 | 16.27 ± 0.13 | 3.125 | 8.27 ± 0.41 | 3.125 | 15.73 ± 0.15 | 12.5 | 5.69 ± 0.17 |
| Au-Ag-TMC-NPs | 0.390 | 24.93 ± 0.09 | 0.781 | 23.56 ± 0.31 | 0.195 | 28.94 ± 0.20 | 3.125 | 7.88 ± 0.22 |
| Marketed antibiotic | 0.781 | 19.86 ± 0.94 | 6.25 | 14.33 ± 0.72 | 0.781 | 20.06 ± 0.53 | 1.562 | 10.38 ± 0.20 |

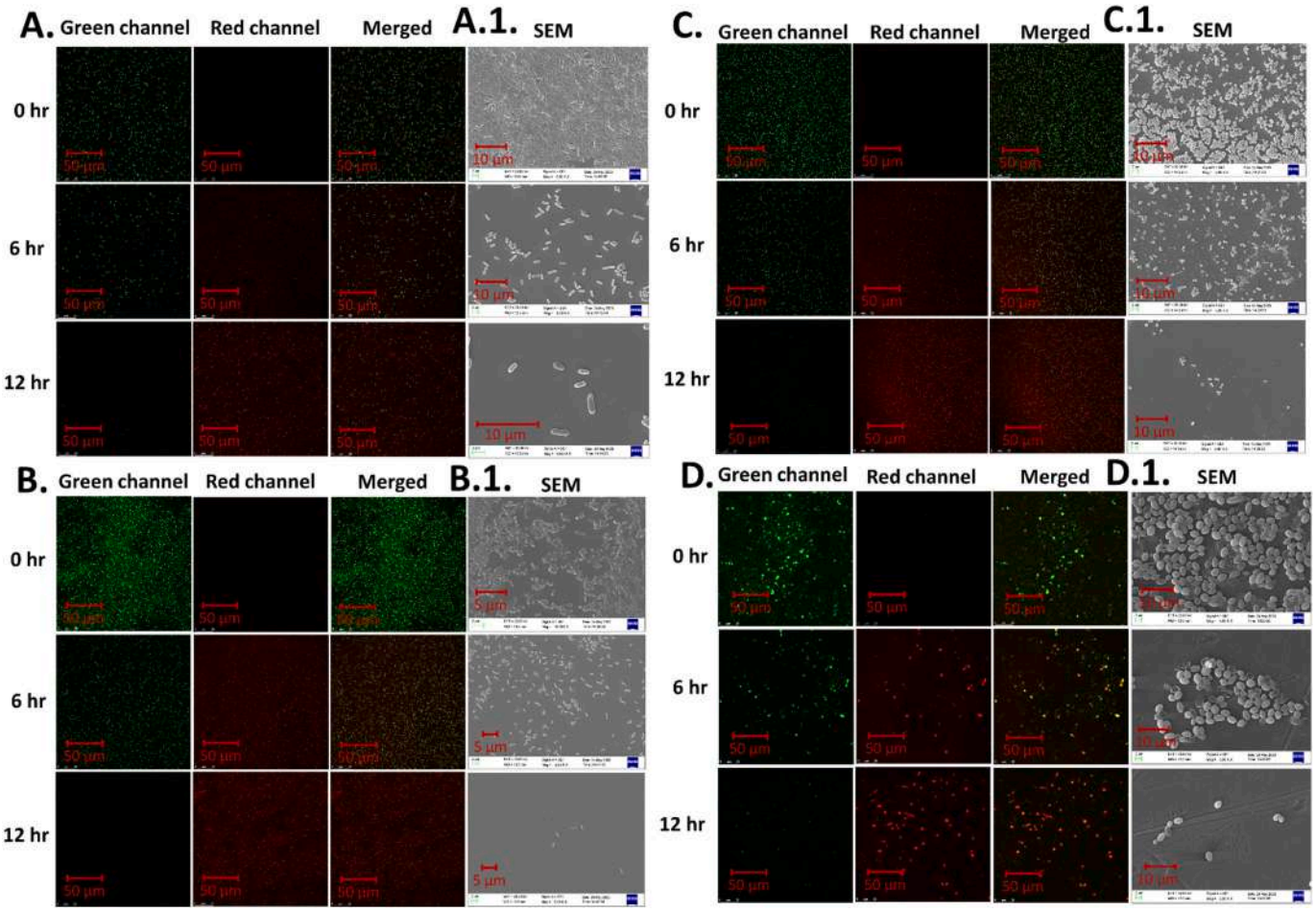


**Fig. 2.** CLSM images of MDR microbial strains after treatment with Au-Ag-TMC-NPs. Co-stained MDR microbial strains (A) *E. coli*; (B) *P. aeruginosa*; (C) *S. aureus* (D) *C. albicans.*

decreased production of certain proteins, potentially reducing the bacterial cell's ability to adapt to its environment, respond to stress, or interact with host organisms in the case of dangerous microbes.

### 3.3. Hemolysis study of nanoparticles

The hemolysis produced by Au-NPs, Au-TMC-NPs, Ag-NPs, Ag-TMC-NPs and Au-Ag-TMC-NPs was compared with distilled water and saline on erythrocytes and was depicted in Fig. S7. The hemolysis (%) induced by distilled water, saline, Au-NPs, Au-TMC-NPs, Ag-NPs, Ag-TMC-NPs and Au-Ag-TMC-NPs was 98.50 ± 1.31 %, 1.57 ± 0.11 %, 2.94 ± 0.11 %, 2.09 ± 0.09 %, 3.54 ± 0.14 %, 2.10 ± 0.09 %, 2.23 ± 0.09 %, 1.24 ± 0.05 % respectively. According to the findings, the nanoparticles repeatedly shown hemolysis levels that were lower than the predetermined threshold of 2 %, which substantiates the fact that they do not display hemolytic properties when they are exposed to human blood [69].

### 3.4. Characterization of nanofibers

#### 3.4.1. Measurement of contact angle

The measured contact angles for blank nanofibers were 36.18 ± 1.64° (left) and 37.52 ± 1.27° (right), whereas the contact angles for Au-Ag-TMC-NPs were 56.54 ± 0.91° (left) and 62.06 ± 1.08° (right) (Fig. 6A and B). The findings demonstrated that hydrophilicity of the electrospun nanofibers was substantially decreased with the addition of Au-Ag-TMC-NPs in nanofibers.

#### 3.4.2. TEM analysis of Au-Ag-TMC-NPs-NFs

The electron micrograph of the fibers showed the diameter ranged in size (diameter) from 100 nm to 350 nm (Fig. 6C, D). The TEM study clearly showed the presence of many Au–Ag-TMC-NPs embedded in the nanofibers which can be seen as black spots on the surface of the nanofibers. Within the context of blank nanofibers, the absence of nanoparticles being embedded or trapped within the nanofiber structure is seen. In contrast, the Au-Ag-TMC-NPs-NFs exhibit nanoparticles ranging in size from 50 nm to 110 nm, alongside nanofibers measuring 304 nm in diameter. It was reported that the diameter of the electrospun nanofibers was dependent on the properties of the electrospinning solution, such as viscosity, electrical conductivity, chemical composition, and molecular weight of the constituent polymers [70,71]. This observation provides evidence for the existence of Au-Ag-TMC-NPs within the nanofibers [72].

#### 3.4.3. SEM analysis of Au-Ag-TMC-NPs-NFs

The morphological analysis indicates the presence of a uniform or homogenous network composed of cross-linked nanofibers, with sizes ranging from 100 to 400 nm (Fig. 6C, D). The material exhibited a persistent and intricate network architecture characterized by interconnected pores in three dimensions in both cases. This findings demonstrated rougher interface architecture which was ascribed to nanofibers mixed on the pore wall, advantageous to both cell adhesion and proliferation.

#### 3.4.4. AFM analysis of Au-Ag-TMC-NPs-NFs

The 2D images of the AFM phase and the 3D images of the AFM

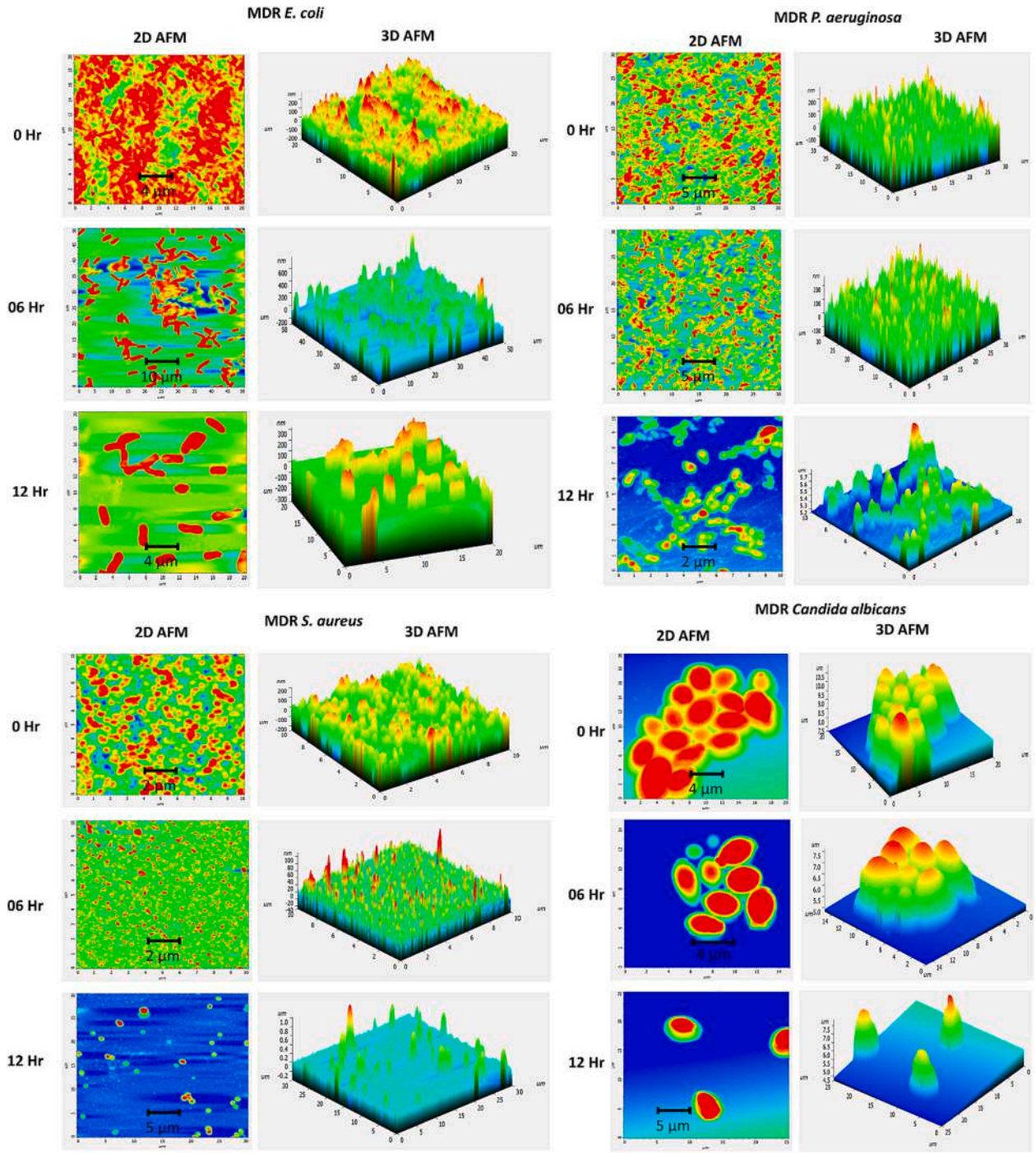


**Fig. 3.** Atomic force microscopy (AFM) study of MDR microbial strain after treatment with Au-Ag-TMC-NPs at different interval of time.

height were acquired utilizing intermittent-contact (tapping) mode (Fig. 6C, D). The samples demonstrated exceptional axial orientation in the fiber architectures, which were characterized by relatively smooth surfaces. No discernible accumulation was detected when Au-Ag-TMC-NPs were adequately situated within the fibers. Furthermore, it has been shown that there are no substantial variations in roughness in either the longitudinal or lateral orientations, indicating that the dispersion of these roughness characteristics within the PVA fibers is satisfactory. The aggregation of certain fibers resulted in the creation of composite structures composed of several fibers. In each instance, the fibers that were prepared resulted in the development of interlaced structures that are accountable for the establishment of quite uniform networks.

### 3.4.5. FT-IR analysis

Broad and prominent peaks about 3400 $cm^{-1}$ were observed for both the samples, corresponding to the stretching vibrations of OH and NH groups (Fig. 6E). The observed phenomenon of the peak's wavenumber shifting towards lower values can be attributed to the increase in PVA/chitosan content within the samples. This shift indicates the formation of hydrogen bonds between the PVA/chitosan and TMC chains. Since PVA contains free hydroxyl group and chitosan has free amine group. So,

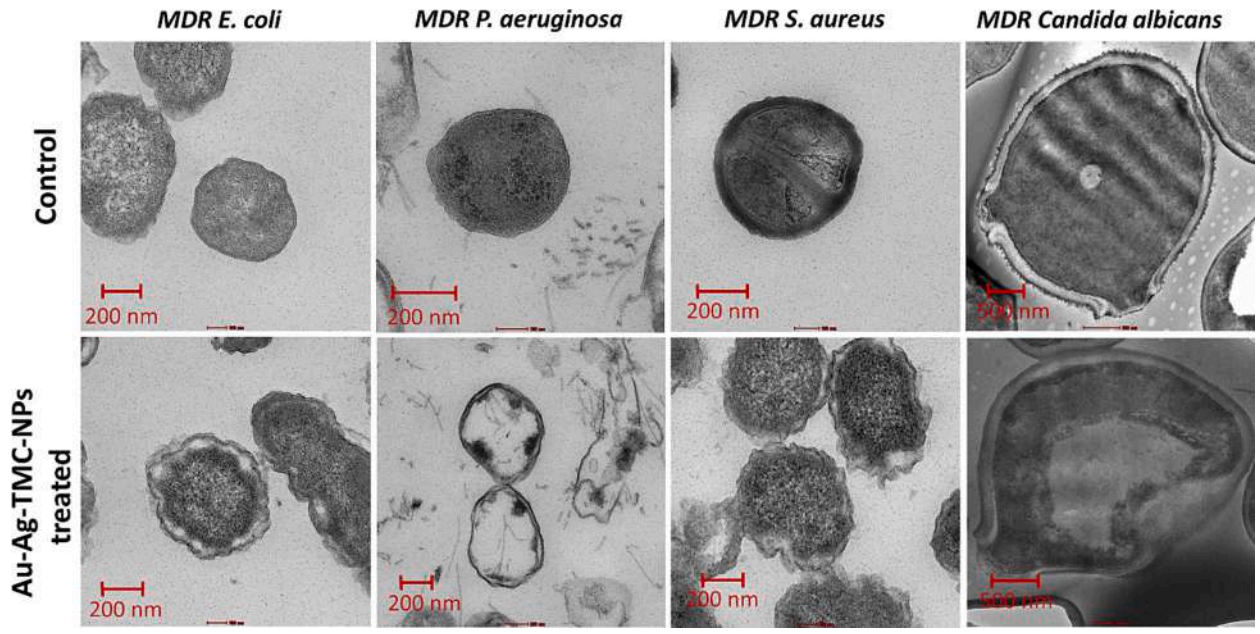


**Fig. 4.** Transmission electron micrograph of MDR microbial strains of Au-Ag-TMC-NPs treated and control.

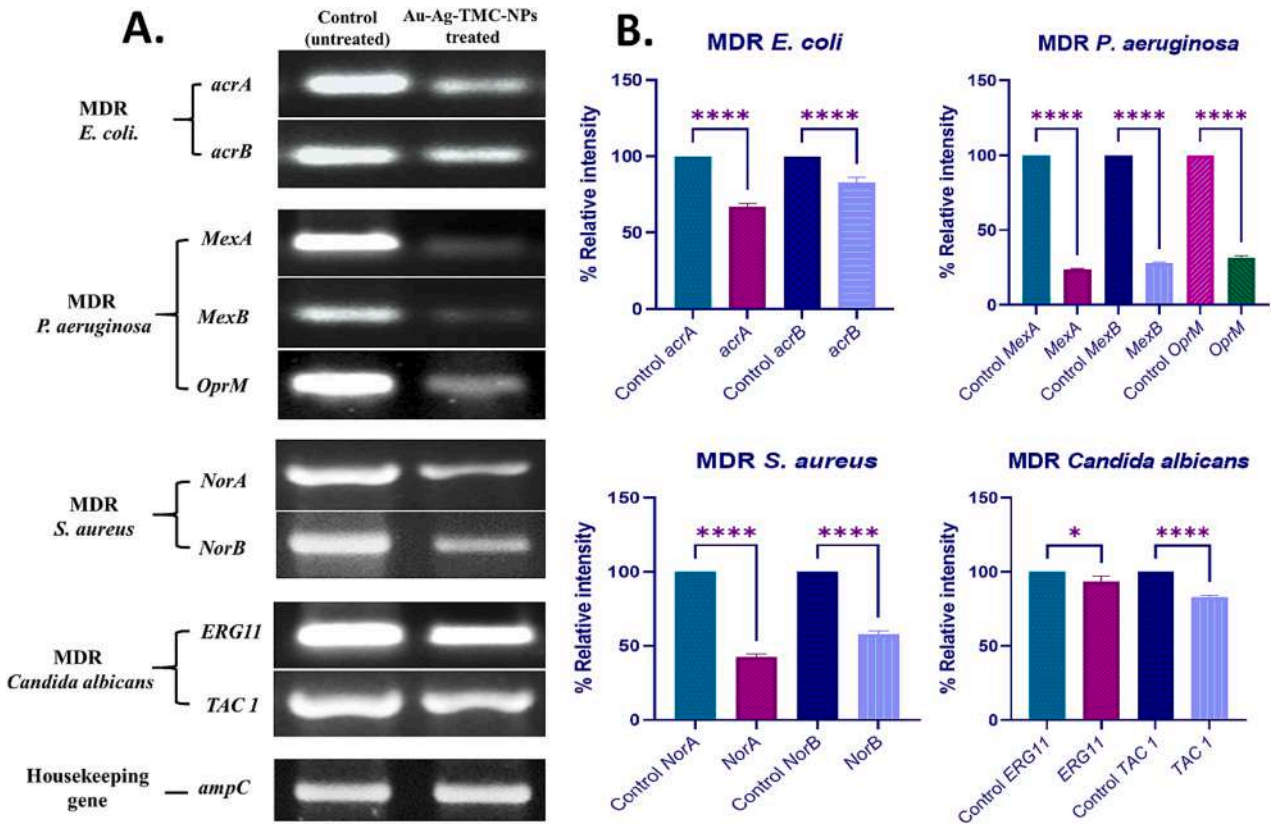


**Fig. 5.** (A) Agrose gel electrophoresis of mRNA expressions of different genes on specific MDR microbes showed that the MDR microbes, after treatment with Au-Ag-TMC-NPs showed differential mRNA expression of genes. It was observed that the expression of all the gene was downregulated after treatment with Au-Ag-TMC-NPs except the gene expressions of *ERG11, TAC1* in MDR *candida albicans* and partially down regulation of *acrA* and *acrB* of MDR *E. coli.* as compared to other expressions of the efflux pump protein (B) Relative % mRNA expression of genes.

there will be possibly inter-molecular H-bonding between chitosan and PVA. The weaker N—H vibration corresponding to the peak around 1560 $cm^{-1}$ found in blank nanofiber was suppressed as the PVA content in the samples was increased. This is further evidence that the PVA can crosslink with TMC chains and form hydrogen bonds. PVA/chitosan containing nanofibers' -$CH_2$- rock band was picked up at 720 $cm^{-1}$. Additionally, these nanofibers exhibited a peak at 845 $cm^{-1}$ that was associated with C—H bond shaking. By loading the nanoparticles in the blank nanofibers, the samples reduced the absorbance of this peak. Vibration of C—O bonds causes the peak at 1100 $cm^{-1}$ in PVA-containing

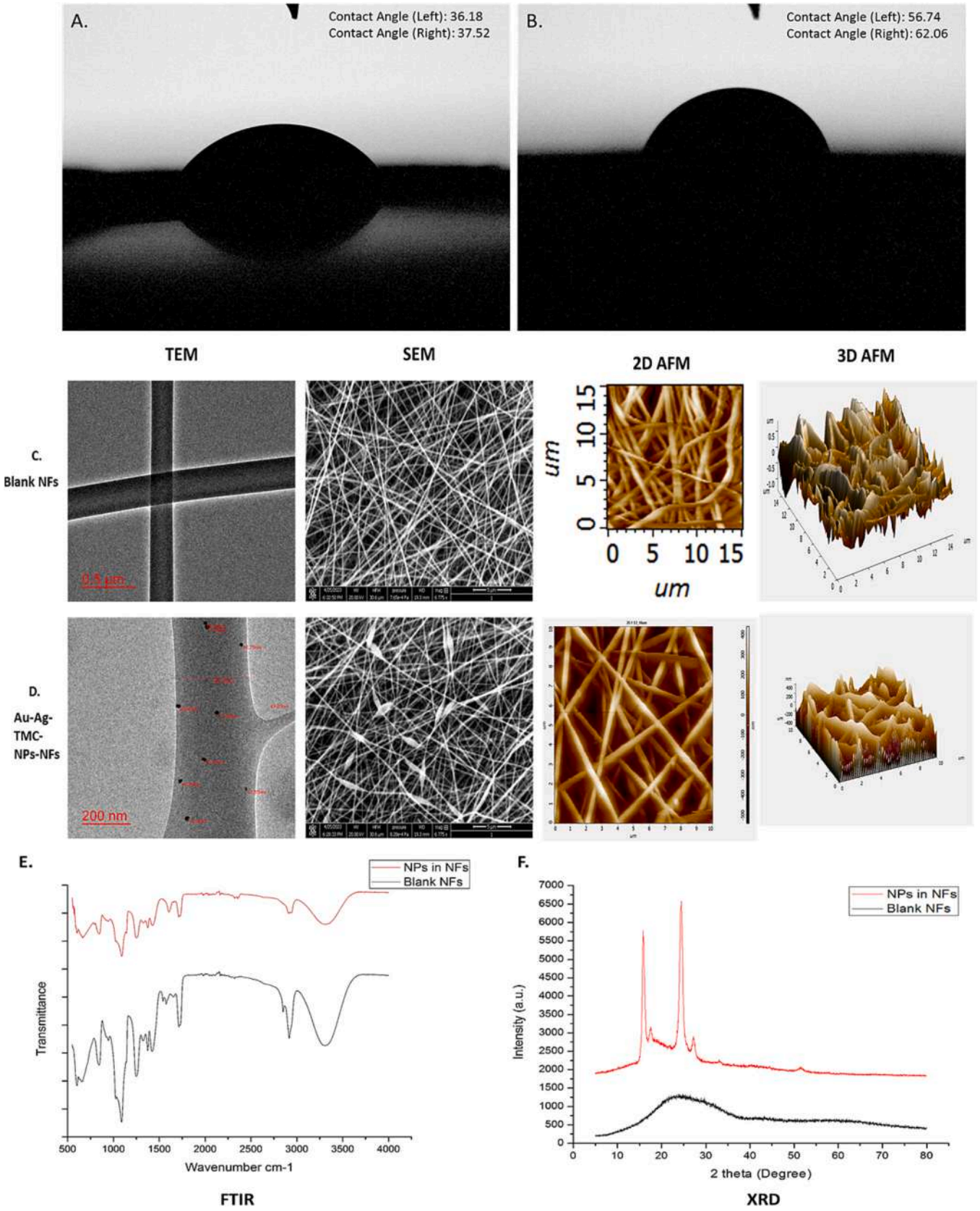


**Fig. 6.** Characterization of nanofibers (A) contact angle of the blank nanofiber (B) contact angle of the nanoparticles loaded nanofibers (C) TEM, SEM, 2D AFM and 3D AFM of blank nanofibers (D) TEM, SEM, 2D AFM and 3D AFM of Au-Ag-TMC-NPs-NFs (E) FT-IR of the nanofibers (F) XRD of nanofibers.

nanofibers. Crystallization of PVA is known to affect this shoulder-appearing peak. C—O stretching vibrations are responsible for the peak at 1260 $cm^{-1}$. PVA's CH-OH and $CH_2$ symmetric bending mode vibrations peaked at 1370 and 1431 $cm^{-1}$, respectively.

### 3.4.6. XRD analysis

XRD is used to analyze the crystallinity in polymeric nanofibers. The XRD spectra of blank fiber showed a broad peak revealing its amorphous nature, whereas the XRD spectra of Au-Ag-TMC-NPs-NF showed sharp peaks at 2θ of 15°, 25° and 28°, which revealed its polycrystalline nature (Fig. 6F). This outcome depicted that the existence of poly-crystallographic orientations inside the nanofiber structure may alter numerous crucial aspects essential to wound healing. For instance, the grain boundaries between crystalline domains may effect the mechanical characteristics of the nanofibers, influencing their flexibility and strength. This may be critical for ensuring that the nanofibrous material responds efficiently to the dynamic and complicated mechanical environment of the healing wound.

### 3.4.7. Thermal stability of nanofibers

The degradation temperature of blank nanofiber and NPs in NFs were recorded be 233.54 °C and 240.41 °C respectively (Fig. S8. A). However, no considerable difference was observed between both the scaffolds.

### 3.4.8. Release study of nanofibers

The in vitro release profile of Au-Ag-TMC-NPs and Au-Ag-TMC-NPs-NF was found to be 95.19 ± 2.55 %, and 25.91 ± 2.12 % after 8 h, respectively (Fig. S8. B). The release profile of Au-Ag-TMC-NPs-NFs showed a slow and prolonged release of the bimetallic complex over 48 h, whereas the release profile of Au-Ag-TMC-NPs showed a rapid and complete release of the bimetallic complex within 12 h. These outcomes suggests that Au-Ag-TMC-NPs-NFs has the potential for sustained release of molecules, while Au-Ag-TMC-NPs could be more appropriate for short-term drug delivery.

### 3.4.9. Hemolysis study of nanofibers

The percentage of hemolysis induced by distilled water, saline, Au-Ag-TMC-NPs and Au-Ag-TMC-NPs-NFs was 98.53 ± 1.43 %, 1.63 ± 0.11 %, 1.24 ± 0.05 % and 1.01 ± 0.06 % respectively, which indicated that the nanofibers were nonhemolytic in nature [69]. This confirms the nanofibers are considered non-hemolytic materials (Fig. S8. C).

### 3.4.10. Nanofibers pH

The dressing pH values of all the blank nanofiber and Au-Ag-TMC-NPs-NFs are 6.95 ± 0.57 and 6.10 ± 0.34 respectively (Fig. S8. D). The nanofibers were designed with an acidic environment to effectively regulate and limit the development of bacteria and the progression of infections. This is because several harmful bacteria flourish in a pH range that is either neutral or slightly alkaline. Additionally, a somewhat acidic pH may facilitate certain elements of the wound healing process, such as the functioning of enzymes responsible for tissue regeneration [73]. Therefore, it was concluded that the acidic Au-Ag-TMC-NPs nanofiber films would furnish an appropriate environment to boost cell proliferation and fibroblast development.

### 3.4.11. Whole blood clotting ability

The Au-Ag-TMC-NPs-NFs film showed a significantly lower absorbance value than blank nanofiber film as well as pure blood, showed their higher blood clotting ability (Fig. S8. E). Blood clotting ability of nanofiber significantly enhanced after addition of bimetallic nanoparticles.

### 3.4.12. Thrombus formation test

Compared to a blank nanofiber film, clot formation was significantly higher when blood met Au-Ag-TMC-NPs-NFs films (Fig. S8. F). Hemostatic assay results showed that the Au-Ag-TMC-NPs-NFs film, with its accelerated blood clotting and thrombus formation abilities, was the most preferable for enhancing hemostasis capabilities.

### 3.4.13. Water retention capacity

The blank nanofiber achieved a weight gain of 713 ± 48 % from its initial weight after being merged in PBS solution for 48 h. While the nanoparticles in nanofibers achieved 1137 ± 83 % weight gain from its initial weight. Hence it is concluded that the Au-Ag-TMC-NPs-NFs has the highest water retention property among them. Since nanofibers have water retention capacity, it signifies that these nanofibrous materials possess the ability to absorb and retain water or aqueous solutions. This property is very essential in wound healing applications.

### 3.4.14. Stability and degradation studies of nanofibers

Stability and degradation of nanofiber was done after 13-days of continuous immersing in PBS. The electrospun nanofibers were found to be stable and show no appreciable degradation. Forceps were still able to grip samples after 10 days of continuous immersing in water. Due to the presence of lysozyme in many bodily fluids, including tears and serum, an in vitro degradation study was performed to mimic the behavior of nanofibers in vivo [74]. Moreover, we found the percentage weight loss in both the nanofibers scaffolds. In particular, blank nanofiber and Au-Ag-TMC-NPs-NFs showed a percentage weight loss of 31.26 ± 1.14 and 8.37 ± 0.53 respectively. This demonstrates the biological stability of the nanofibers to assure compatibility with live tissues and cells, preventing undesirable responses or disintegration.

## 3.5. Wound healing potential study of Au-Ag-TMC-NPs-NFs

The wound healing activity of Au-Ag-TMC-NPs-NFs was recorded up to 12 days as day 1, day 4, day 8 and day 12. There was an observation made that untreated mice wounds showed unhealed (Fig. 7A). Au-Ag-TMC-NPs-NFs accelerated the wound closure in the group which is infected by MDR *P. aeruginosa* followed by uninfected wound + Au-Ag-TMC-NPs-NFs then *E. coli* infected + Au-Ag-TMC-NPs-NFs then uninfected + marketed formulation followed by *S. aureus* + Au-Ag-TMC-NPs-NFs and in infected group the delayed healing is observed in *Candida albicans* infected wound treated by Au-Ag-TMC-NPs-NFs, further this investigation is supported by the histopathological study of wounds (Fig. 7B). The fastest wound healing percentage rate is 99.34 of MDR *P. aeruginosa* infected wound treated by Au-Ag-TMC-NPs-NFs (Fig. 7C). Therefore, the Au-Ag-TMC-NPs-NFs + MDR *P. aeruginosa* infected wound healing has better efficacy in comparison to the other groups. The wound healing process exhibits variations in response to distinct bacterial strains, as the onset of chronicity in wounds is initiated by the sustained presence of specific bacteria at the tissue level. Particularly, the production of endotoxins contributes to an extended elevation of proinflammatory cytokines such as interleukin-1 and tumor necrosis factor-α. Consequently, this condition leads to heightened levels of matrix metalloproteases and diminished levels of their tissue inhibitors, accompanied by a reduced production of growth factors. While inflammation is a inherent component of the wound healing mechanism, an excessively heightened inflammatory response can protract the repair process. Bacteria indeed play a significant role in facilitating a controlled inflammatory response during the normal process of wound healing. Subinfective levels of bacteria seem to expedite the healing of wounds and the development of granulation tissue. This acceleration is characterized by heightened infiltration of neutrophils, monocytes, and macrophages, elevated levels of prostaglandin E2, and an augmentation in collagen formation.

Furthermore, there have been reports indicating that the integration of metallic nanoparticles into the polymeric matrix of TMC has shown a significant inhibitory impact on bacterial growth [75]. The antibacterial impact of metallic nanoparticles and their associated ions primarily involves the disruption of biofilm components and their structural integrity and the inhibition of bacterial metabolism via several mechanisms

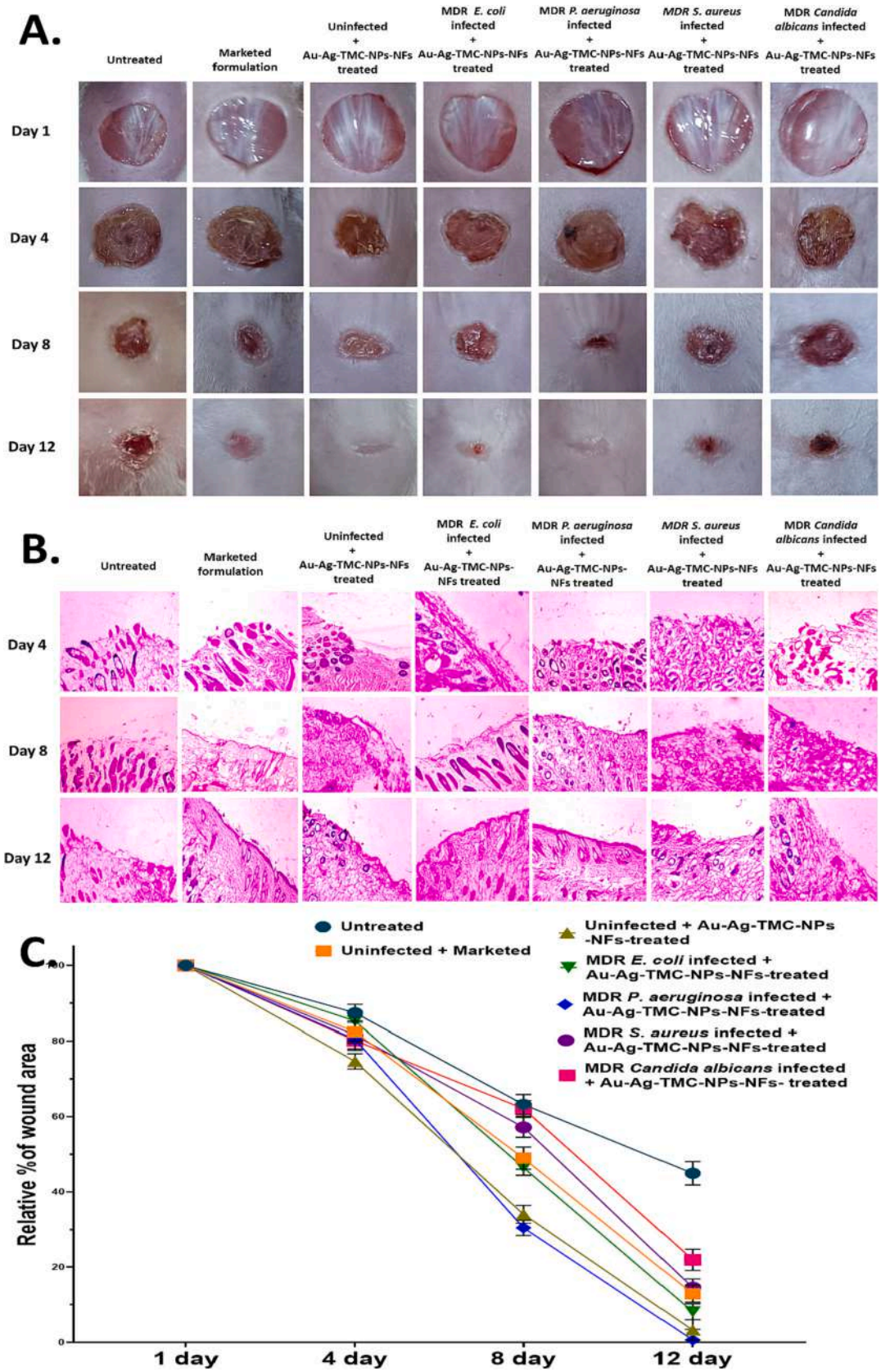


**Fig. 7.** (A) Reduction of wound in mice (B) Skin histological studied under brightfield microscope (at 100× magnification) 4th day, 8th day and 12th day. (C) Graphical representation of relative percent of wound area of different treatment group of animals.

[76]. It signifies that these Au-Ag-TMC-NPs nanofibrous materials, presumably functioning as wound dressings or scaffolds, display powerful antimicrobial activities, especially against MDR strains that have gained resistance to several drugs. The integration of TMC and silver nanoparticles into nanofibers boosts their antibacterial activity, and this has numerous implications for wound care applications. Also, this approach has proven the novelty to improve wound healing without any unwanted consequences.

### 3.6. Western blot study of wound healing marker protein

Healing of the wound requires re-epithelialization that involves proliferation along with migration of the epidermal keratinocytes that surround the wound. To migrate over the wound these keratinocytes undergo an epithelial-to-mesenchymal transition (EMT) process, which is characterized by a phenotypic change of the adherent epithelial cells to a dynamic state [77,78]. These include the re-organization of the cytoskeleton, the decrease in the expression of epithelial junctional components, and the increase in the expression of genes responsible for facilitating cytoskeletal modifications and adhesion to mesenchymal cells [79,80]. To study the process of wound healing via EMT upon application of Au-Ag-TMC-NPs-NFs, we checked the expression of the mesenchymal marker Vimentin by western blotting (Fig. 8A). Vimentin is an intermediate filament that has been reported in various studies to be consistently upregulated during the process of EMT. Further, it is one of the robust markers having prognostic values to indicate EMT [81,82]. Protein lysate was prepared from the wound skin tissues of uninfected mice, and microbial infected mice (MDR strains of *E. coli, P. aeruginosa, S. aureus, and C. albicans*) treated with Au-Ag-TMC-NPs-NFs. Protein lysate from untreated mice, and mice treated with marketed formulation served as the control samples. The expression of Vimentin was found to be significantly upregulated in wounds of *P. aeruginosa* infected mice treated with Au-Ag-TMC-NPs-NFs compared to the untreated control sample. Vimentin expression was also found to be increased in wounds of MDR *E. coli* infected and uninfected mice treated with the nanoparticle, whereas samples from MDR *S. aureus* and *C. albicans* infected mice upon treatment with the nanoparticle showed no to very mild expression of Vimentin. Mice treated with marketed formulation also showed a significant expression of Vimentin. Our observations suggested that the application of Au-Ag-TMC-NPs-NFs accelerated wound healing via EMT in MDR *P. aeruginosa*, MDR *E. coli* infected and uninfected mice as evident from the increased expression level of Vimentin in these protein samples.

Transforming growth factor-beta (TGF-β) signaling has been acknowledged to be a key player in inducing EMT during wound healing and keratinocyte migration [83]. Activation of TGF-β leads to the

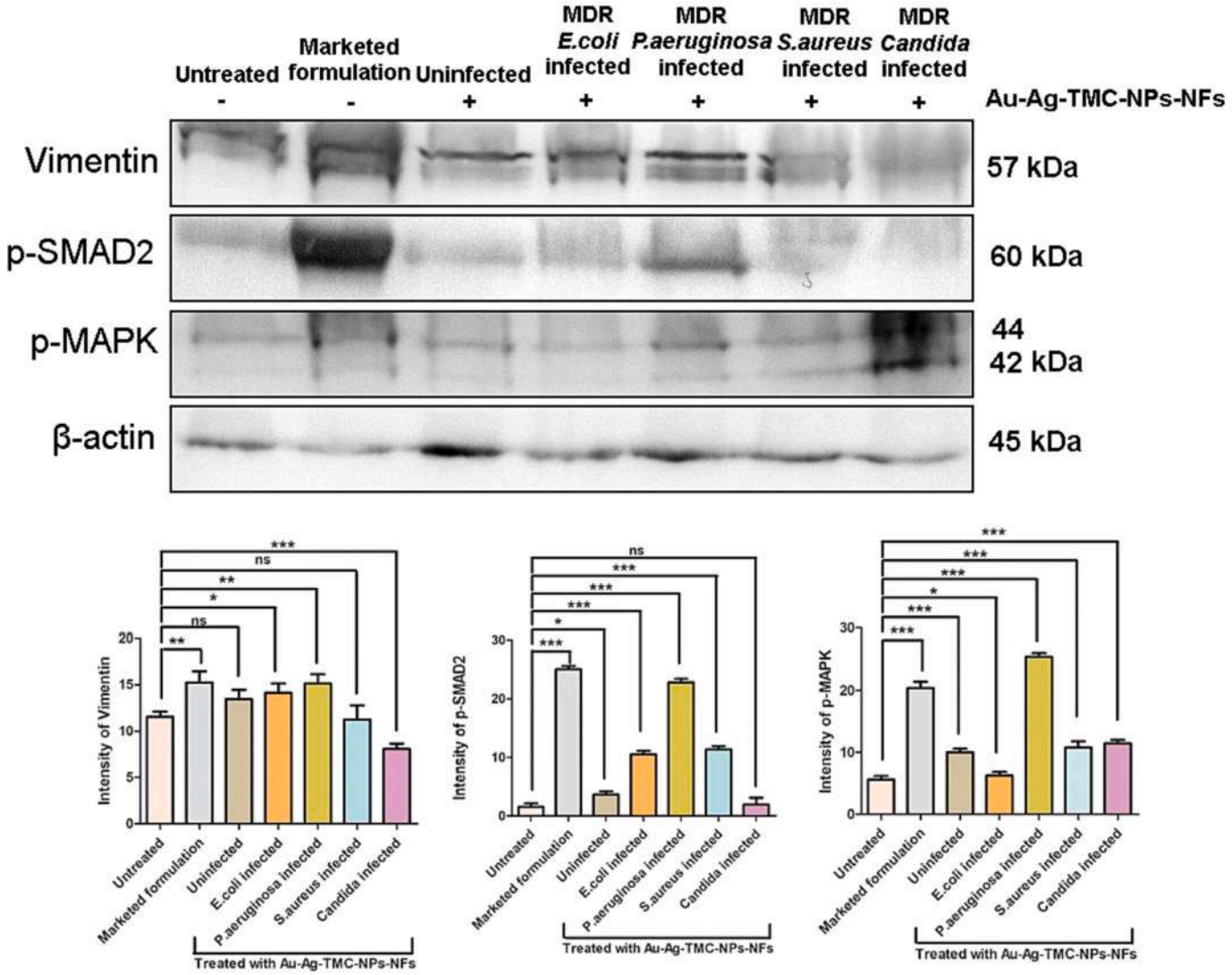


**Fig. 8.** (A) Au-Ag-TMC-NPs-NFs accelerate wound healing in mice via inducing EMT and activation of TGF-β and ERK pathways (B) Relative % wound marker expressions.

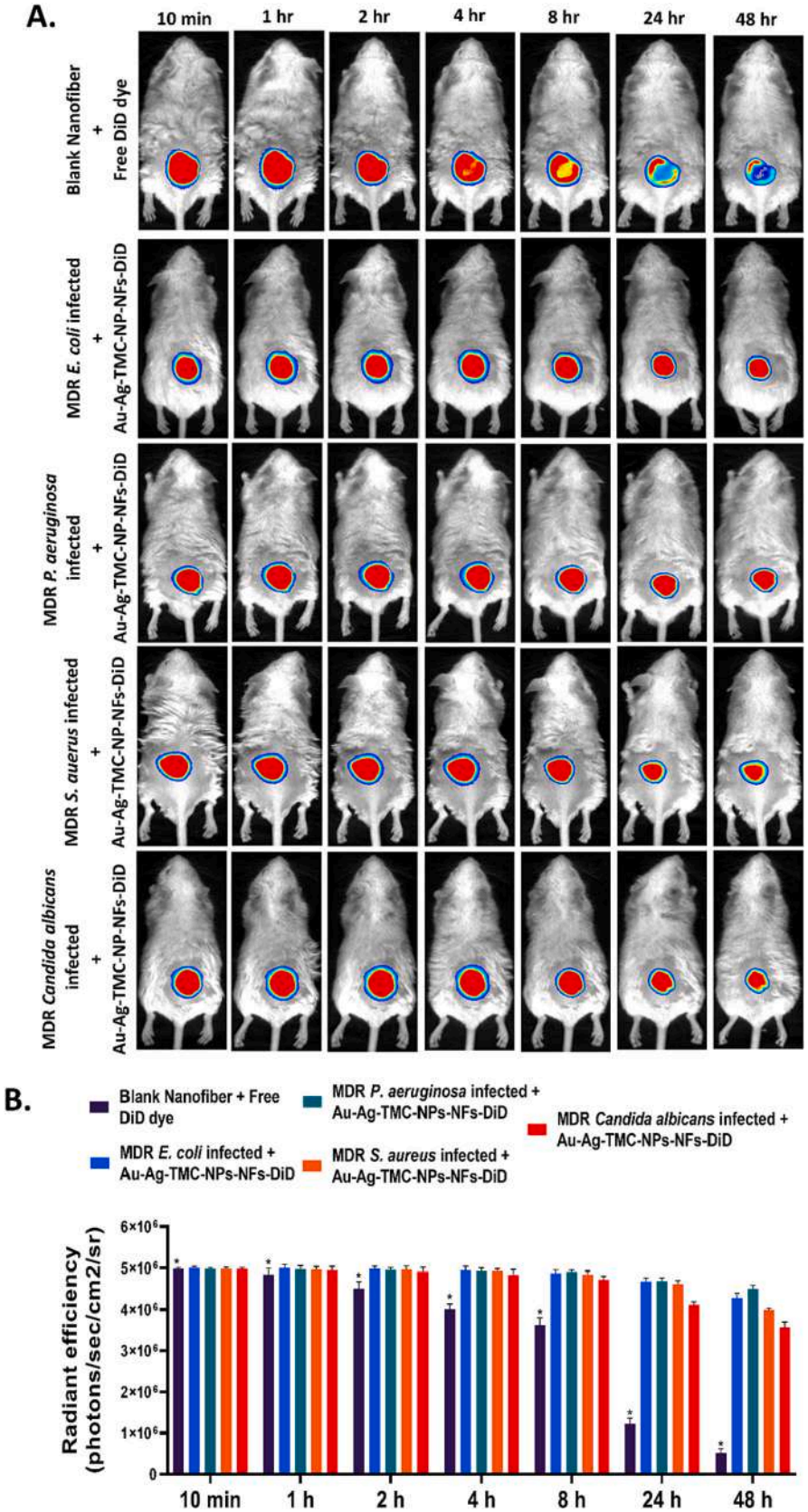


**Fig. 9.** In vivo live optical imaging (A) In vivo biodistribution of free-DiD from blank nanofiber (as control) and Au-Ag-TMC-NPs-NF-DiD while infected with different microbes within 48 h of application at 10 min., 1, 2, 4, 8, 24, and 48 h post-treatment (B) CLSM Confocal microscopy of Blank nanofiber + Free DiD dye.

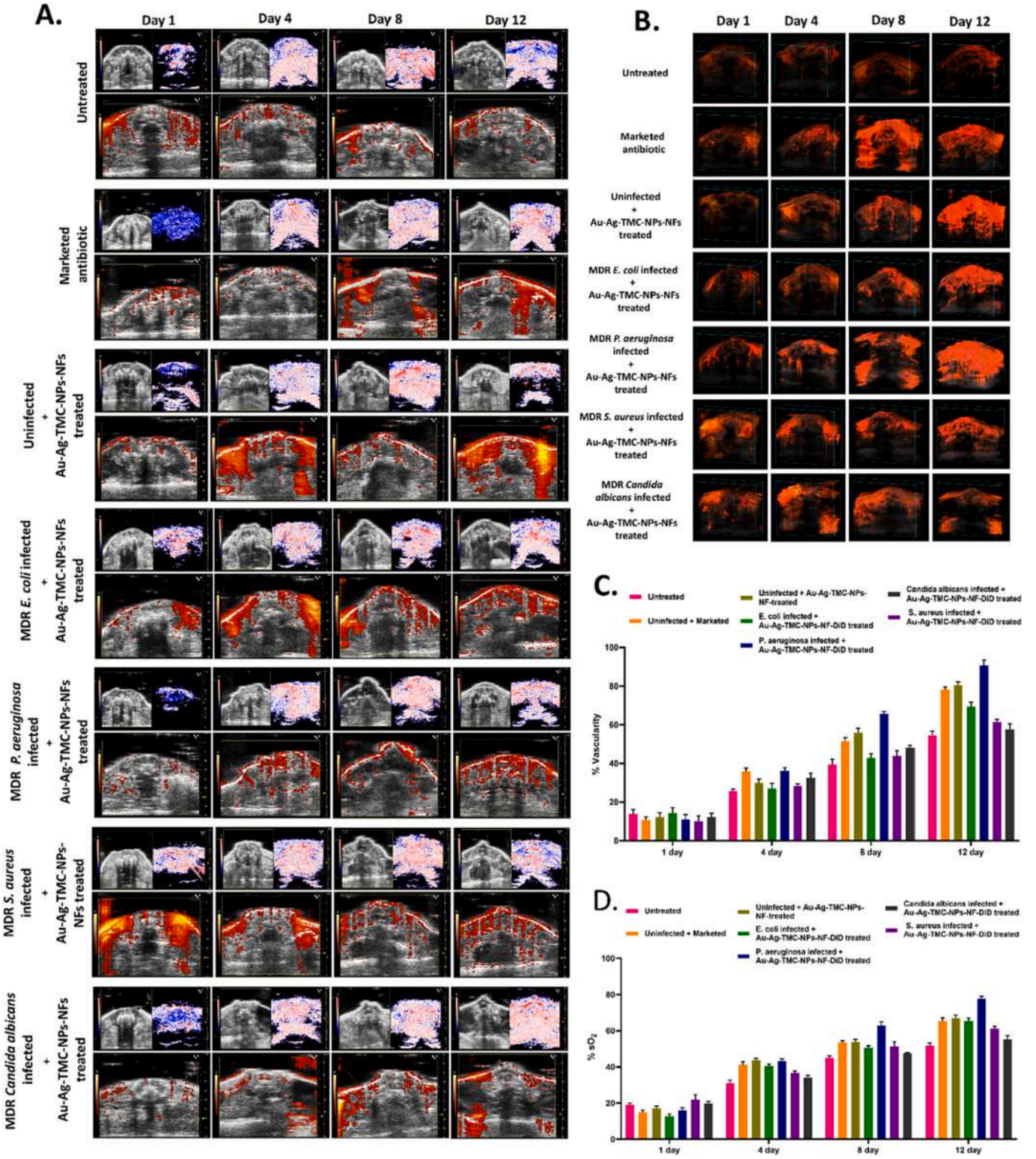


**Fig. 10.** (A) Ultrasound and photoacoustic imaging of the wound of respective groups (B) Power doppler images of the wound of respective groups (C) Percentage vascularity of the wound of respective animal groups (D) $SO_2$% of the wound of respective animal groups.

phosphorylation of downstream signaling molecules SMAD2/3 that subsequently leads to transcription of genes involved in cell proliferation and migration [84]. TGF-β signaling has been reported to induce the expression of Vimentin, thereby leading to the process of EMT [85]. To determine the status of TGF-β signaling known to promote EMT, we assessed the expression status of its downstream signaling component phosphorylated SMAD2 via western blotting in the mice samples. SMAD2 was found to be highly phosphorylated in *P. aeruginosa* infected mice treated with Au-Ag-TMC-NPs-NFs and mice treated with the marketed formulation. This was evident from the increased expression level of p-SMAD2 in both these experimental samples. Reduced expression of p-SMAD2 was observed in the other samples. Our findings indicated that

TGF-β was upregulated in MDR *P. aeruginosa* infected mice treated with Au-Ag-TMC-NPs-NFs. Activation of TGF-β indicated an accelerated wound healing in MDR *P. aeruginosa* infected mice treated with Au-Ag-TMC-NPs-NFs.

According to various studies, it is now established that signaling pathways cross-talk extensively to carry out distinct biological functions. TGF-β has been shown to interact with mitogen activated protein kinases (MAPKs) that regulate the secretion of growth factors and cytokines that promote EMT [86,87]. MAPKs are protein Ser/Thr kinases that coordinately dictate cell proliferation, differentiation, cell motility and survival. Studies conducted by Davies and the group represents the MAPKs function to enhance SMAD2/3 dependent transcription during TGF-β induced EMT. One of the conventional MAPKs consists extracellular signal-regulated kinases 1 and 2 (ERK1/2) [87]. Davies et al. demonstrated that MAPKs enhanced SMAD2 dependent transcription leading to promotion of EMT [87]. Since p-MAPKs have been reported to regulate TGF-β signaling via regulating phosphorylation of SMAD2, we also studied the expression status of p-MAPK (ERK1/2) in wound healing in mice upon application of Au-Ag-TMC-NPs-NFs. At this end, phosphorylation of MAPK was more significant in MDR *P. aeruginosa* infected and uninfected mice treated with Au-Ag-TMC-NPs-NFs, as evident from the increased band intensity obtained in these samples compared to other samples. The signaling pathways MAPKs and TGF-β known to regulate EMT have also been suggested to be upregulated in our studies as evident from the expression pattern of p-SMAD2 and p-MAPKs [86]. Here, activation of p-MAPK might indicate a promotion of EMT, thus leading to accelerated wound healing. Our observations suggested that Au-Ag-TMC-NPs-NFs generated in our lab accelerate wound healing in mice via promoting EMT, as evident from the increased expression of the mesenchymal marker Vimentin and this process is being regulated by the activation of the signaling pathways TGF-β and pMAPK (ERK1/2). The Fig. 8B represents the band intensities of Vimentin, p-SMAD2 and p-MAPK in wound inflicted uninfected and microbe infected mice treated with the nanofibers carrying nanoparticles. The untreated mice served as the negative control and the mice treated with marketed formulation served as the positive control. The expression of these markers were consistently found to elevated in MDR *P. aeruginosa* infected mice treated with Au-Ag-TMC-NPs-NFs. Expression of these markers were observed to be mildly increased in uninfected and MDR *E. coli* infected mice treated with Au-Ag-TMC-NPs-NFs whereas a negligible expression was observed in mice infected with MDR *S. aureus* and MDR *C. albicans* treated with the nanoparticles. This suggested that the application of Au-Ag-TMC-NPs-NFs generated in our lab-accelerated wound healing in *P. aeruginosa* infected mice. An unpaired *t*-test was conducted in order to get the *p*-value (ns-not significant, $*p < 0.05$, $**p < 0.01$, $***p < 0.001$).

### 3.7. In-vivo nanoformulation release study

The IVIS study demonstrated the indirect quantification of the rate of biodistribution of nanoparticles over the time (Fig. 9A). Here, the release of free DiD from blank nanofiber (control) (Fig. S9A) and Au-Ag-TMC-NPs-NF-DiD (Fig. S9B) while infected with different microbes within 48 h of application. The release was examined at time intervals of 10 min., 1, 2, 4, 8, 24, and 48 h post-treatment. The intensity of the DiD dye fluorescence is measured as the radiant efficiency (photons/s/cm$^2$/sr). It has been found that DiD is rapidly released from blank nanofiber with free DiD beginning 4 h after administration with a significant decrease in the fluorescent signals and disappearing completely 48 h later. On the other hand, the nanofibers with DiD tagged nanoparticles (Au-Ag-TMC-NPs-NFs-DiD) exhibited a sustained release of the DiD dye with a slow decrease in fluorescent signals, which provides an understanding of the release of nanoparticles at wound sites over a long period of time with effective treatment. These results confirm the sustained delivery of nanomaterial at infected wound sites over a prolonged period, triggering a positive therapeutic impact (Fig. 9B).

### 3.8. In-vivo ultrasound/photoacoustic study

Photoacoustic imaging of the MDR microbial infected wound of mice was recorded at 1 day and at 4$^{th}$ day, 8$^{th}$ day, and 12$^{th}$ day after treatments (Fig. 10A). The ultrasound/PA images indicated a notable improvement in the healing process of the infected wound following the implementation of nanofibers. The blood flow in all the respective groups was studied by using the power doppler method (Fig. 10B). The percentage vascularity (Fig. 10C) changes on 12$^{th}$ day of infected wound healing were 54.56 ± 2.10, 78.15 ± 1.28, 80.45 ± 1.70, 69.45 ± 2.13, 90.66 ± 2.79, 61.56 ± 1.26 and 57.63 ± 2.78 for untreated, uninfected-marketed, uninfected, MDR *E. coli* infected Au-Ag-TMC-NPs-NFs treated, MDR *P. aeruginosa* infected Au-Ag-TMC-NPs-NFs treated, MDR *S. aureus* infected Au-Ag-TMC-NPs-NFs treated, and MDR *C. albicans* infected Au-Ag-TMC-NPs-NFs treated groups respectively. Photoacoustic (PA) imaging was used to assess the changes % $sO_2$ (Fig. 10D). The $sO_2$ percentage changes on 12$^{th}$ day of infected wound healing were 51.64 ± 1.60, 65.36 ± 1.78, 69.98 ± 1.70, 65.98 ± 1.64, 77.64 ± 1.43, 61.20 ± 1.26 and 55.17 ± 1.98 for untreated, uninfected-marketed, uninfected, MDR *E. coli* infected Au-Ag-TMC-NPs-NFs treated, MDR *P. aeruginosa* infected Au-Ag-TMC-NPs-NFs treated, MDR *S. aureus* infected Au-Ag-TMC-NPs-NFs treated, and MDR *C. albicans* infected Au-Ag-TMC-NPs-NFs treated groups respectively. The provided (Fig. 10C) displays representative maximum intensity projections of wound healing pictures acquired using 3D power Doppler. The provided photos offer a qualitative representation of the blood flow intensity observed on day 1 and on days 4, 8, and 12 following the therapy. The vascular index was employed to quantitatively assess the relative alterations in blood flow within the wound.

Outcome of in vivo ultrasound/photoacoustic study indicates that the rate of wound healing is significantly higher in MDR *P. aeruginosa* infected wounds treated with Au-Ag-TMC-NPs-NFs compared to uninfected wounds. Additionally, the healing rate is higher in uninfected wounds treated with a commercially available formulation compared to MDR *E. coli* infected wounds treated with Au-Ag-TMC-NPs-NFs. Furthermore, MDR *S. aureus* infected wounds treated with Au-Ag-TMC-NPs-NFs exhibits a faster healing rate compared to MDR *Candida albicans* infected wounds treated with the same nanoparticles. Lastly, the slowest rate of healing is observed in untreated wounds. Because the persistence of certain microbes at the tissue level is what causes wounds to become chronic, the healing process varies depending on the kind of microbial infection present.

## 4. Conclusion

The research emphasises the versatility of TMC with bimetallic nanoparticles and how it may be used as an agent for accelerated MDR microbial infected wound healing approach with no adverse effects over available marketed formulations. The developed Au-Ag-TMC-NPs downregulates the efflux pump gene expressions in MDR microbes. The synthesized wound dressing with Au-Ag-TMC-NPs was found to have sustained release of therapeutic agents on wound sites with accelerated healing within 12 days. The molecular findings by western blotting indicates that the wound dressing exhibits enhanced efficacy in stimulating collagen deposition and may have accelerated the process of wound healing. Furthermore, the real time wound visualization, angiogenesis, vascularity, and wound oxygen saturation by ultrasound/photoacoustic imaging system supports the improved oxygen saturation, increased vascularity and enhanced degree of wound closure. However, this study is limited to the isolated MDR microbial strains from the local hospitals, and a single therapeutic delivery system was used, although in future the other possible delivery systems can be explored with the isolated MDR microbial strains from different sites globally. Overall, the Au-Ag-TMC-NPs-NFs wound dressing can lay the foundation for the development of future antibacterial and antifungal agents with significant wound-healing potential.

## CRediT authorship contribution statement

**Ankit Kumar Malik:** Conceptualization, Investigation, Methodology, Writing – review & editing, Writing – original draft. **Chandrashekhar Singh:** Writing – review & editing, Methodology, Data curation. **Punit Tiwari:** Formal analysis, Data curation. **Dipti Verma:** Writing – review & editing, Visualization, Methodology. **Abhishesh Kumar Mehata:** Writing – original draft, Methodology, Investigation. **Vikas:** Writing – review & editing, Visualization, Validation. **Aseem Setia:** Writing – review & editing. **Ashim Mukherjee:** Writing – review & editing. **Madaswamy S. Muthu:** Writing – review & editing, Project administration.

## Declaration of competing interest

The authors declare that they have no known competing financial interests or personal relationships that could have appeared to influence the work reported in this paper.

## Data availability

All data that support the findings of this study are included within the article (and any supplementary files).

## Acknowledgments

The authors are grateful to the Prime Minister's Research Fellowship Scheme, Ministry of Education, Government of India for granting PMRF. IIT(BHU)/Scheme (PMRF)/2022-23/2646. Furthermore, we would like to express our gratitude to SATHI-BHU, Varanasi for granting us access to the Ultrasound and Photoacoustic imaging facility, as well as the Laser Scanning Super Resolution Microscope System. We are also thankful to CIF-IIT BHU for their assistance in the instrumental characterization of nanoparticles. Lastly, we extend our appreciation to the All India Institute of Medical Sciences (AIIMS), Delhi for their support in conducting bacterial TEM microscopy.

## Appendix A. Supplementary data

Supplementary data to this article can be found online at https://doi.org/10.1016/j.ijbiomac.2024.130154.

## References

[1] T. Xu, M. Xin, M. Li, H. Huang, S. Zhou, Synthesis, characteristic and antibacterial activity of N, N, N-trimethyl chitosan and its carboxymethyl derivatives, Carbohydr. Polym. 81 (2010) 931–936.
[2] Y.A. Alli, O. Ejeromedoghene, A. Oladipo, S. Adewuyi, S.A. Amolegbe, H. Anuar, S. Thomas, Compressed hydrogen-induced synthesis of quaternary trimethyl chitosan-silver nanoparticles with dual antibacterial and antifungal activities, ACS Appl. Bio Mater. 5 (2022) 5240–5254.
[3] P. Sahariah, D. Cibor, D. Zielińska, M. Hjálmarsdóttir, D. Stawski, M. Másson, The effect of molecular weight on the antibacterial activity of N,N,N-Trimethyl Chitosan (TMC), Int. J. Mol. Sci. 20 (2019).
[4] M. Avadi, A. Sadeghi, A. Tahzibi, K. Bayati, M. Pouladzadeh, M. Zohuriaan-Mehr, M. Rafiee-Tehrani, Diethylmethyl chitosan as an antimicrobial agent: synthesis, characterization and antibacterial effects, Eur. Polym. J. 40 (2004) 1355–1361.
[5] A. Anisiei, B.I. Andreica, L. Mititelu-Tartau, C.G. Coman, R. Bilyy, G. Bila, I. Rosca, A.I. Sandu, E. Amler, L. Marin, Biodegradable trimethyl chitosan nanofiber mats by electrospinning as bioabsorbable dressings for wound closure and healing, Int. J. Mol. Sci. 249 (2023) 126056.
[6] P. Sahariah, G.I. Kontogianni, E. Scoulica, O.E. Sigurjonsson, M. Chatzinikolaidou, Structure-activity relationship for antibacterial chitosan carrying cationic and hydrophobic moieties, Carbohydr. Polym. 312 (2023) 120796.
[7] X. Liu, L. Song, L. Li, S. Li, K. Yao, Antibacterial effects of chitosan and its water-soluble derivatives on *E. coli*, plasmids DNA, and mRNA, J. Appl. Polym. Sci. 103 (2007) 3521–3528.
[8] M.J. Mitcheltree, A. Pisipati, E.A. Syroegin, K.J. Silvestre, D. Klepacki, J.D. Mason, D.W. Terwilliger, G. Testolin, A.R. Pote, K.J.Y. Wu, R.P. Ladley, K. Chatman, A. S. Mankin, Y.S. Polikanov, A.G. Myers, A synthetic antibiotic class overcoming bacterial multidrug resistance, Nature 599 (2021) 507–512.
[9] J. O'Neill, Tackling Drug-Resistant Infections Globally: Final Report and Recommendations, 2016.
[10] J.J.R.A.R. O'neill, Antimicrobial Resistance: Tackling A Crisis for The Health and Wealth of Nations, 2014.
[11] Global burden of bacterial antimicrobial resistance in 2019: a systematic analysis, Lancet (London, England) 399 (2022) 629–655.
[12] H.C. Chen, V. Gau, D.D. Zhang, J.C. Liao, F.Y. Wang, P.K. Wong, Statistical metamodeling for revealing synergistic antimicrobial interactions, PloS One 5 (2010) e15472.
[13] A. Zida, S. Bamba, A. Yacouba, R. Ouedraogo-Traore, R.T. Guiguemdé, Anti-Candida albicans natural products, sources of new antifungal drugs: a review, JMM 27 (2017) 1–19.
[14] B. Yu, C. He, W. Wang, Y. Ren, J. Yang, S. Guo, Y. Zheng, X. Shi, Asymmetric wettable composite wound dressing prepared by electrospinning with bioinspired micropatterning enhances diabetic wound healing, ACS Appl. Bio Mater. 3 (2020) 5383–5394.
[15] R. Xu, M. Zhang, J. Yao, Y. Wang, Y. Ge, D. Kremenakova, J. Militky, G. Zhu, Highly antibacterial electrospun double-layer mats for preventing secondary wound damage and promoting unidirectional water conduction in wound dressings, J. Ind. Eng. Chem. 119 (2023) 404–413.
[16] C. Xie, J. Yan, S. Cao, R. Liu, B. Sun, Y. Xie, K. Qu, W. Zhang, Z. Weng, Z. Wang, Bi-layered disulfiram-loaded fiber membranes with antibacterial properties for wound dressing, Appl. Biochem. Biotechnol. 194 (2022) 1359–1372.
[17] D. MubarakAli, N. Thajuddin, K. Jeganathan, M. Gunasekaran, Plant extract mediated synthesis of silver and gold nanoparticles and its antibacterial activity against clinically isolated pathogens, Colloids Surf. B. 85 (2011) 360–365.
[18] A. Mushtaq, M.Z. Iqbal, X.J. Kong, Antiviral effects of coinage metal-based nanomaterials to combat COVID-19 and its variants, J. Mater. Chem. B. 10 (2022) 5323–5343.
[19] G. Franci, A. Falanga, S. Galdiero, L. Palomba, M. Rai, G. Morelli, M. Galdiero, Silver nanoparticles as potential antibacterial agents, Molecules (Basel, Switzerland) 20 (2015) 8856–8874.
[20] R. Vazquez-Muñoz, A. Meza-Villezcas, P.G.J. Fournier, E. Soria-Castro, K. Juarez-Moreno, A.L. Gallego-Hernández, N. Bogdanchikova, R. Vazquez-Duhalt, A. Huerta-Saquero, Enhancement of antibiotics antimicrobial activity due to the silver nanoparticles impact on the cell membrane, PloS One 14 (2019) e0224904.
[21] S.M. Mousavi, S.M.A. Mousavi, M. Moeinizadeh, M. Aghajanidelavar, S. Rajabi, M. Mirshekar, Evaluation of biosynthesized silver nanoparticles effects on expression levels of virulence and biofilm-related genes of multidrug-resistant Klebsiella pneumoniae isolates, J. Basic Microbiol. 63 (2023) 632–645.
[22] Y. Wu, L. Zhang, Y. Zhou, Y. Li, Q. Liu, J. Hu, J. Yang, Light-induced ZnO/Ag/rGO bactericidal photocatalyst with synergistic effect of sustained release of silver ions and enhanced reactive oxygen species, Chinese J. Catal. 40 (2019) 691–702.
[23] S. Zhang, R. Fu, D. Wu, W. Xu, Q. Ye, Z. Chen, Preparation and characterization of antibacterial silver-dispersed activated carbon aerogels, Carbon 42 (2004) 3209–3216.
[24] C. Singh, A.K. Mehata, P. Tiwari, A. Setia, A.K. Malik, S.K. Singh, R. Tilak, M. S. Muthu, Design of novel bioadhesive chitosan film loaded with bimetallic gold-silver nanoparticles for antibiofilm and wound healing activity, Biomed. Mater. 18 (2023) 025014.
[25] A.K. Mehata Vikas, M.K. Viswanadh, A.K. Malik, A. Setia, P. Kumari, S.K. Mahto, M.S. Muthu, EGFR targeted redox sensitive chitosan nanoparticles of cabazitaxel: dual-targeted cancer therapy, lung distribution, and targeting studies by photoacoustic and optical imaging, Biomacromolecules 24 (2023) 4989–5003.
[26] E. Korzeniewska, A. Korzeniewska, M. Harnisz, Antibiotic resistant Escherichia coli in hospital and municipal sewage and their emission to the environment, Ecotoxicol. Environ. Saf. 91 (2013) 96–102.
[27] P.P. Preeja, S.H. Kumar, V. Shetty, Prevalence and characterization of methicillin-resistant *staphylococcus aureus* from community- and hospital-associated infections: a tertiary care center study, Antibiotics (Basel, Switzerland) 10 (2021).
[28] R. Skov, R. Smyth, A. Larsen, A. Bolmstrom, A. Karlsson, K. Mills, N. Frimodt-Moller, G. Kahlmeter, Phenotypic detection of methicillin resistance in Staphylococcus aureus by disk diffusion testing and Etest on Mueller-Hinton agar, J. Clin. Microbiol. 44 (2006) 4395–4399.
[29] H. Yan, C. Liu, W. Yu, X. Zhu, B. Chen, The aggregate distribution of Pseudomonas aeruginosa on biochar facilitates quorum sensing and biofilm formation, Sci. Total Environ. 856 (2023) 159034.
[30] S. Beg, A.K. Malik, M.J. Ansari, A.A. Malik, A.M.A. Ali, A. Theyab, M. Algahtani, W. H. Almalki, K.S. Alharbi, S.K. Alenezi, M.A. Barkat, M. Rahman, H. Choudhry, Systematic development of solid lipid nanoparticles of abiraterone acetate with improved oral bioavailability and anticancer activity for prostate carcinoma treatment, ACS Omega 7 (2022) 16968–16979.
[31] I. Maliszewska, A. Zdubek, On the photo-eradication of methicillin-resistant staphylococcus aureus biofilm using methylene blue, Int. J. Mol. Sci. 24 (2023).
[32] J. Liu, F. Chen, X. Wang, H. Peng, H. Zhang, K.J. Wang, The synergistic effect of mud crab antimicrobial peptides sphistin and sph(12-38) with antibiotics azithromycin and rifampicin enhances bactericidal activity against Pseudomonas aeruginosa, Front. Cell. Infect. 10 (2020) 572849.
[33] A.M. Shehabeldine, B.H. Amin, F.A. Hagras, A.A. Ramadan, M.R. Kamel, M. A. Ahmed, K.H. Atia, S.S. Salem, Potential antimicrobial and antibiofilm properties of copper oxide nanoparticles: time-kill kinetic essay and ultrastructure of pathogenic bacterial cells, Appl. Biochem. Biotechnol. 195 (2023) 467–485.
[34] H. Li, H. Liu, L. Zhang, A. Hieawy, Y. Shen, Evaluation of extracellular polymeric substances matrix volume, surface roughness and bacterial adhesion property of oral biofilm, J. Dent. Sci. 18 (2023) 1723–1730.

[35] V.A. Carneiro, S.T. de Oliveira, R.L. Silva, H. de Sousa Duarte, M.L. Silva, M.N. C. Matos, R.M.B. Cavalcante, C.S. Figueira, E.N. Lorenzón, E.M. Cilli, R.M.S. da Cunha, Antimicrobial and antibiofilm activity of lys-[trp6]hy-a1 combined with ciprofloxacin against gram-negative bacteria, Protein Pept. Lett. 27 (2020) 1124–1131.

[36] B. Pourakbari, S. Yaslianifard, S. Yaslianifard, S. Mahmoudi, S. Keshavarz-Valian, S. Mamishi, Evaluation of efflux pumps gene expression in resistant Pseudomonas aeruginosa isolates in an Iranian referral hospital, Iran. J. Microbiol. 8 (2016) 249–256.

[37] H. Savli, A. Karadenizli, F. Kolayli, S. Gundes, U. Ozbek, H. Vahaboglu, Expression stability of six housekeeping genes: a proposal for resistance gene quantification studies of Pseudomonas aeruginosa by real-time quantitative RT-PCR, J. Med. Microbiol. 52 (2003) 403–408.

[38] *Escherichia coli* serotype O73 AcrA (acrA) gene, partial cds - Nucleotide - NCBI. (n.d.) https://www.ncbi.nlm.nih.gov/nuccore/HQ833334.1, (2024).

[39] *Escherichia coli* strain AF45 AcrB (acrB) gene, partial cds - Nucleotide - NCBI. (n.d.). https://www.ncbi.nlm.nih.gov/nuccore/MT956578, (2023).

[40] *Pseudomonas aeruginosa* strain ARD-7 MexA (mexA) gene, partial cds - Nucleotide - NCBI. (n.d.). https://www.ncbi.nlm.nih.gov/nuccore/ON920994.1, (2023).

[41] mexB multidrug resistance protein MexB [*Pseudomonas aeruginosa* PAO1] - Gene - NCBI. (n.d.). https://www.ncbi.nlm.nih.gov/gene/877852, (2023).

[42] S.S. Costa, B. Sobkowiak, R. Parreira, J.D. Edgeworth, M. Viveiros, T.G. Clark, I. Couto, Genetic diversity of nora, coding for a main efflux pump of staphylococcus aureus, Front. Genet. 9 (2018) 710.

[43] *Staphylococcus aureus* strain S16 multidrug efflux MFS transporter nor - Nucleotide - NCBI. (n.d.). https://www.ncbi.nlm.nih.gov/nuccore/MN013174.1, (2023).

[44] K. Gołąbek, J.K. Strzelczyk, A. Owczarek, P. Cuber, A. Ślemp-Migiel, A. Wiczkowski, Selected mechanisms of molecular resistance of Candida albicans to azole drugs, Acta Biochim. Pol. 62 (2015) 247–251.

[45] *Candida albicans* Tac1 (Tac1) gene, complete cds - Nucleotide - NCBI. (n.d.). https://www.ncbi.nlm.nih.gov/nuccore/OQ383350.1?report=genbank&to=2946, (2023).

[46] *Pseudomonas aeruginosa* strain ARD-53 AmpC (ampC) gene, partial cds - Nucleotide - NCBI. (n.d.). https://www.ncbi.nlm.nih.gov/nuccore/ON920993.1, (2023).

[47] S.K. Rout, V. Priya, A.K. Mehata, M.S. Muthu, Technology, Abciximab coated albumin nanoparticles of rutin for improved and targeted antithrombotic effect, J Drug Del Sci Tech 76 (2022) 103785.

[48] M. Koosha, H. Mirzadeh, Electrospinning, mechanical properties, and cell behavior study of chitosan/PVA nanofibers, J. Biomed. Mater. Res.. Part A 103 (2015) 3081–3093.

[49] V.R. Viana, W.H. Ferreira, E.G. Azero, M.L. Dias, C.T. Andrade, Optimization of the electrospinning conditions by box-behnken design to prepare poly (vinyl alcohol)/chitosan crosslinked nanofibers, J. Mater. Sci. Chem. Eng. 8 (2020) 13.

[50] S.M. Hosseini, F. Moradi, S.K. Farahani, S. Bandehali, F. Parvizian, M. Ebrahimi, J. Shen, Carbon nanofibers/chitosan nanocomposite thin film for surface modification of poly (ether sulphone) nanofiltration membrane, Mater. Chem. Phys. 269 (2021) 124720.

[51] N. Varshney, A.K. Sahi, S. Poddar, S.K. Mahto, Soy protein isolate supplemented silk fibroin nanofibers for skin tissue regeneration: fabrication and characterization, Int. J. Biol. Macromol. 160 (2020) 112–127.

[52] H. Xu, Z. Wu, D. Zhao, H. Liang, H. Yuan, C. Wang, Preparation and characterization of electrospun nanofibers-based facial mask containing hyaluronic acid as a moisturizing component and huangshui polysaccharide as an antioxidant component, Int. J. Biol. Macromol. 214 (2022) 212–219.

[53] M.A. Wsoo, S.I.A. Razak, S.P.M. Bohari, S. Shahir, R. Salihu, M.R.A. Kadir, N.H. M. Nayan, Vitamin D(3)-loaded electrospun cellulose acetate/polycaprolactone nanofibers: characterization, in-vitro drug release and cytotoxicity studies, Int. J. Biol. Macromol. 181 (2021) 82–98.

[54] M. Bacalum, M. Radu, Cationic antimicrobial peptides cytotoxicity on mammalian cells: an analysis using therapeutic index integrative concept, Int. J. Pept. Res. Ther. 21 (2015) 47–55.

[55] S. Samadieh, A. Dehnad, B. Naghili, M. Sadri, A. Bazmani, Hemocompatibility assessment and drug release kinetics investigation from materials based on electrospun nanofibers, J. Nanomed. Res. 4 (2019) 10–15.

[56] S.Y. Ong, J. Wu, S.M. Moochhala, M.H. Tan, J. Lu, Development of a chitosan-based wound dressing with improved hemostatic and antimicrobial properties, Biomaterials 29 (2008) 4323–4332.

[57] R.K. Dey, A.R. Ray, Synthesis, characterization, and blood compatibility of polyamidoamines copolymers, Biomaterials 24 (2003) 2985–2993.

[58] Y. Zheng, F. Jiang, C. Wang, M. Dong, C. Wang, E. Yan, Y. Wang, Z. Zhu, X. Xiong, X. Ding, J. Ye, Y. He, H. Zhang, J. Zhou, W. Zhang, Y. Wu, X. Song, Regulation of Semaphorin3A in the process of cutaneous wound healing, Cell Death Differ. 29 (2022) 1941–1954.

[59] R. Swann, S. Slikboer, A. Genady, L.R. Silva, N. Janzen, A. Faraday, J.F. Valliant, S. Sadeghi, Tetrazine-derived near-infrared dye for targeted photoacoustic imaging of bone, J. Med. Chem. 66 (2023) 6025–6036.

[60] A. Singh, R. Ghosh, P. Guchhait, CXCR3 antagonist rescues ER stress and reduces inflammation and JEV infection in mice brain, Cytokine 172 (2023) 156380.

[61] J.D. Clogston, A.K. Patri, Zeta potential measurement, Methods Mol. Biol. (Clifton, N.J.) 697 (2011) 63–70.

[62] S. Kumar, R.K. Majhi, A. Singh, M. Mishra, A. Tiwari, S. Chawla, P. Guha, B. Satpati, H. Mohapatra, L. Goswami, C. Goswami, Carbohydrate-coated gold-silver nanoparticles for efficient elimination of multidrug resistant bacteria and in vivo wound healing, ACS Appl. Mater. Interfaces 11 (2019) 42998–43017.

[63] M.E. Levison, Pharmacodynamics of antimicrobial drugs, Infect. Dis. Clin. North Am. 18 (2004) 451–465 (vii).

[64] T.J. Beveridge, Structures of gram-negative cell walls and their derived membrane vesicles, J. Bacteriol. 181 (1999) 4725–4733.

[65] C. Singh, A.K. Mehata, V. Priya, A.K. Malik, A. Setia, M.N.L. Suseela, P. Gokul Vikas, S.K. Samridhi, M.S. Muthu Singh, Bimetallic Au-Ag nanoparticles: advanced nanotechnology for tackling antimicrobial resistance, Molecules (Basel, Switzerland) (2022) 27.

[66] M. Ramasamy, J.H. Lee, J. Lee, Potent antimicrobial and antibiofilm activities of bacteriogenically synthesized gold-silver nanoparticles against pathogenic bacteria and their physiochemical characterizations, J. Biomater. Appl. 31 (2016) 366–378.

[67] R. Banasiuk, J.E. Frackowiak, M. Krychowiak, M. Matuszewska, A. Kawiak, M. Ziabka, Z. Lendzion-Bielun, M. Narajczyk, A. Krolicka, Synthesis of antimicrobial silver nanoparticles through a photomediated reaction in an aqueous environment, Int. J. Nanomedicine 11 (2016) 315–324.

[68] F. Botha, I. Elisha, A. Jambalang, C. Van der Merwe, C. Baker, J. Eloff, Evaluation of the antifungal mode of action of cremaspora triflora on *candida albicans* using sem and tem.

[69] J. Choi, V. Reipa, V.M. Hitchins, P.L. Goering, R.A. Malinauskas, Physicochemical characterization and in vitro hemolysis evaluation of silver nanoparticles, Toxicol. Sci. 123 (2011) 133–143.

[70] J.A. Lopes-da-Silva, B. Veleirinho, I. Delgadillo, Preparation and characterization of electrospun mats made of PET/chitosan hybrid nanofibers, J. Nanosci. Nanotechnol. 9 (2009) 3798–3804.

[71] A. Al-Abduljabbar, I. Farooq, Electrospun polymer nanofibers: processing, properties, and applications, Polymers 15 (2022).

[72] F. Gentile, L. Tirinato, E. Battista, F. Causa, C. Liberale, E.M. di Fabrizio, P. Decuzzi, Cells preferentially grow on rough substrates, Biomaterials 31 (2010) 7205–7212.

[73] K. Skórkowska-Telichowska, M. Czemplik, A. Kulma, J. Szopa, The local treatment and available dressings designed for chronic wounds, JAAD 68 (2013) e117–e126.

[74] D. Ren, H. Yi, W. Wang, X. Ma, The enzymatic degradation and swelling properties of chitosan matrices with different degrees of N-acetylation, Carbohydr. Res. 340 (2005) 2403–2410.

[75] M. Lopez-Carrizales, E. Mendoza-Mendoza, R.D. Peralta-Rodriguez, M.A. Pérez-Díaz, D. Portales-Pérez, M. Magaña-Aquino, A. Aragón-Piña, R. Infante-Martínez, E.D. Barriga-Castro, R. Sánchez-Sánchez, G.A. Martinez-Castañon, F. Martinez-Gutierrez, Characterization, antibiofilm and biocompatibility properties of chitosan hydrogels loaded with silver nanoparticles and ampicillin: an alternative protection to central venous catheters, Colloids Surf. B. 196 (2020) 111292.

[76] Q. Li, F. Lu, G. Zhou, K. Yu, B. Lu, Y. Xiao, F. Dai, D. Wu, G. Lan, Silver inlaid with gold nanoparticle/chitosan wound dressing enhances antibacterial activity and porosity, and promotes wound healing, Biomacromolecules 18 (2017) 3766–3775.

[77] C.E. Weber, N.Y. Li, P.Y. Wai, P.C. Kuo, Epithelial-mesenchymal transition, TGF-β, and osteopontin in wound healing and tissue remodeling after injury, J. Burn Care Res. 33 (2012) 311–318.

[78] R. Vu, M. Dragan, P. Sun, S. Werner, X. Dai, Epithelial-mesenchymal plasticity and endothelial-mesenchymal transition in cutaneous wound healing, Cold Spring Harb. Perspect. Biol. 15 (2023).

[79] G.D. Marconi, L. Fonticoli, T.S. Rajan, S.D. Pierdomenico, O. Trubiani, J. Pizzicannella, F. Diomede, Epithelial-mesenchymal transition (emt): the type-2 emt in wound healing, tissue regeneration and organ fibrosis, Cells 10 (2021).

[80] D. Haensel, X. Dai, Epithelial-to-mesenchymal transition in cutaneous wound healing: where we are and where we are heading, Dev. Dyn. 247 (2018) 473–480.

[81] D.S. Masson-Meyers, T.A.M. Andrade, G.F. Caetano, F.R. Guimaraes, M.N. Leite, S. N. Leite, M.A.C. Frade, Experimental models and methods for cutaneous wound healing assessment, Int. J. Exp. Pathol. 101 (2020) 21–37.

[82] F. Cheng, Y. Shen, P. Mohanasundaram, M. Lindström, J. Ivaska, T. Ny, J. E. Eriksson, Vimentin coordinates fibroblast proliferation and keratinocyte differentiation in wound healing via TGF-β-slug signaling, PNAS 113 (2016) E4320–E4327.

[83] P.V. Peplow, M.P. Chatterjee, A review of the influence of growth factors and cytokines in in vitro human keratinocyte migration, Cytokine 62 (2013) 1–21.

[84] J. Zavadil, M. Bitzer, D. Liang, Y.C. Yang, A. Massimi, S. Kneitz, E. Piek, E. P. Bottinger, Genetic programs of epithelial cell plasticity directed by transforming growth factor-beta, PNAS 98 (2001) 6686–6691.

[85] K. Yoshida, T. Saito, A. Kamida, K. Matsumoto, K. Saeki, M. Mochizuki, N. Sasaki, T. Nakagawa, Transforming growth factor-β transiently induces vimentin expression and invasive capacity in a canine mammary gland tumor cell line, Res. Vet. Sci. 94 (2013) 539–541.

[86] T. Gui, Y. Sun, A. Shimokado, Y. Muragaki, The roles of mitogen-activated protein kinase pathways in TGF-β-induced epithelial-mesenchymal transition, J. Signal Transduct. 2012 (2012) 289243.

[87] M. Davies, M. Robinson, E. Smith, S. Huntley, S. Prime, I. Paterson, Induction of an epithelial to mesenchymal transition in human immortal and malignant keratinocytes by TGF-beta1 involves MAPK, Smad and AP-1 signalling pathways, J. Cell. Biochem. 95 (2005) 918–931.

# Update

International Journal of Biological Macromolecules
Volume 277, Issue P3, October 2024, Page

DOI: https://doi.org/10.1016/j.ijbiomac.2024.134420

International Journal of Biological Macromolecules 277 (2024) 134420

Contents lists available at ScienceDirect

International Journal of Biological Macromolecules

journal homepage: www.elsevier.com/locate/ijbiomac

Corrigendum

# Corrigendum to "Nanofibers of *N*,*N*,*N*-trimethyl chitosan capped bimetallic nanoparticles: Preparation, characterization, wound dressing and in vivo treatment of MDR microbial infection and tracking by optical and photoacoustic imaging" [Int. J. Biol. Macromol. 263 (2024) 130154]

Ankit Kumar Malik [a], Chandrashekhar Singh [a], Punit Tiwari [b], Dipti Verma [c], Abhishesh Kumar Mehata [a], Vikas [a], Aseem Setia [a], Ashim Mukherjee [c], Madaswamy S. Muthu [a,*]

[a] *Department of Pharmaceutical Engineering and Technology, Indian Institute of Technology (BHU), Varanasi 221005, UP, India*
[b] *Department of Microbiology, Institute of Medical Sciences, BHU, Varanasi 221005, UP, India*
[c] *Department of Molecular and Human Genetics, Institute of Science, Banaras Hindu University, Varanasi 221005, UP, India*

The authors regret a mistake, which was entirely unintentional and occurred during the final stages of figure preparation. Specifically, during the data consolidation and visualization process, due to a labelling mistake in our repository of the same animal group, the 7B Untreated Day 4 images were mistakenly over-copied in the **7B Untreated Day 12** folder and the experimental results for **Untreated Day 12** was inadvertently selected. Despite our thorough review processes though typically rigorous, we failed to catch this error by our naked eyes due to the compressed timeframe and multiple concurrent reviews. We have prepared a corrected version of Fig. **7B Untreated Day 12** which accurately reflects our findings and data discussed in the article, whereas the **7B Untreated Day 4** data is correct.

DOI of original article: https://doi.org/10.1016/j.ijbiomac.2024.130154.
* Corresponding author.
*E-mail address:* msmuthu.phe@itbhu.ac.in (M.S. Muthu).

https://doi.org/10.1016/j.ijbiomac.2024.134420

Available online 4 August 2024

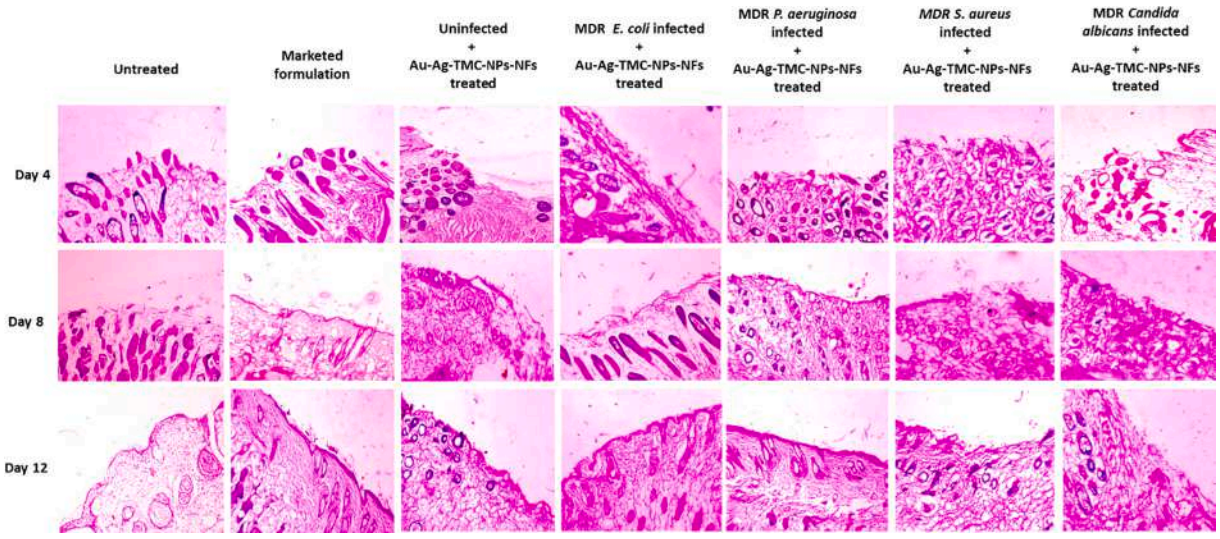


Fig. 7: (B) Skin histological studied under brightfield microscope (at 100× magnification) 4th day, 8th day and 12th day.

The authors would like to apologise for any inconvenience caused.